

Full length article

Dislocation-pinning and dynamic strain-aging in hydrogen-alloyed Fe-Cr-Ni austenitic steel at sub-ambient temperatures

Yuhei Ogawa^{a,*}, Tatsuya Ito^b, Haruki Nishida^{a,c}, Osamu Takakuwa^d, Kaneaki Tsuzaki^{a,d}, Stefanus Harjo^e, Akinobu Shibata^{a,f}

^a Research Center for Structural Materials, National Institute for Materials Science (NIMS), 1-2-1 Sengen, Tsukuba, 305-0047, Japan

^b Department of Materials Science, Tohoku University, 6-6-02 Aramaki-Aoba, Aoba-ku, Sendai, 980-8579, Japan

^c Graduate School of Science and Technology, University of Tsukuba, 1-1-1 Tennodai, Tsukuba, Ibaraki, 305-8577 Japan

^d Department of Mechanical Engineering, Kyushu University, 744 Motoooka, Nishi-ku, Fukuoka, 819-0395, Japan

^e J-PARC Center, Japan Atomic Energy Agency (JAEA), 2-4 Shirakata, Tokai-mura, Naka-gun, Ibaraki, 319-1195, Japan

^f Institute of Pure and Applied Sciences, University of Tsukuba, 1-1-1 Tennodai, Tsukuba, Ibaraki, 305-8577 Japan

ARTICLE INFO

Keywords:

Austenitic steels

Hydrogen

Dislocations

Dynamic strain-aging

Stress relaxation

ABSTRACT

The interaction between solute hydrogen (H) and mobile dislocations in Fe-24Cr-19Ni mass% (Type310S) austenitic steel charged with 8500 atomic ppm H was investigated by stress relaxation tests conducted over the temperature range 213–295 K. At ambient condition, H atoms form solute atmospheres that can migrate coordinately with moving dislocations. In contrast, the reduced H diffusivity at lower temperatures progressively impedes dislocation motion, leading to dynamic strain aging (DSA) during the relaxation process, manifested as a retardation of thermally activated deformation. As a direct consequence of this dislocation-pinning effect, a pronounced yield point emerged upon reloading after relaxation. The kinetics of solute atmosphere formation and DSA were further quantified by evaluating the exhaustion rate of mobile dislocation density as a function of relaxation time. The experimental trends were successfully described using a classical Cottrell atmosphere model based on size-misfit interaction, demonstrating that the fundamental role of H in governing dislocation mobility is essentially analogous to that of other interstitial solute elements.

1. Introduction

When interstitial solute atoms—most notably carbon (C), nitrogen (N), and hydrogen (H)—are introduced into face-centered cubic (FCC) metals and alloys, they give rise to solid solution-hardening through a combination of static and dynamic interaction mechanisms with dislocations [1–8]. Statistically, the local lattice dilatation around interstitial solutes generates elastic stress fields that interact with those of dislocations, thereby acting as short-range (*i.e.*, thermally activatable) obstacles against dislocation motion [1,9,10]. In addition to such a static contribution, diffusible interstitials can dynamically interact with moving dislocations, also leading to time- and temperature-dependent strengthening phenomena [4,6,11]. The resulting increase in yield and flow stresses during plastic deformation is therefore governed not only by solute concentration but also by thermomechanical loading conditions, reflecting the thermally activated dislocation motion [12,13] and the relative velocity of dislocations to solute diffusion kinetics [14–16].

These multifaceted effects underscore the complexity of solute–dislocation interactions in determining the rate-controlling processes of plasticity.

Recently, the authors have investigated the role of solute H in governing dislocation dynamics in Fe-Cr-Ni-based austenitic stainless steels [17–20]. Particular attention was devoted to tensile deformation behavior at ambient temperature where H atoms are exceptionally mobile [8,21]. Under sufficiently low strain rates (*e.g.*, below 10^{-4} /s), H atoms were found to dynamically segregate to moving dislocations and form solute atmospheres, in a manner analogous to other alloying elements at elevated temperatures [14–16,22–24]. The migration of these H-decorated dislocations was identified as a primary origin of solid solution-hardening, with the H residing in dislocation core playing a decisive role in impeding dislocations motion [17,19]. In particular, each incremental glide advance of a dislocation core requires the concurrent migration of segregated H via atomic diffusion jumps—diffusion-controlled glide [12,23,25]. This activation process of H

* Corresponding author.

E-mail address: OGAWA.Yuhei@nims.go.jp (Y. Ogawa).

<https://doi.org/10.1016/j.actamat.2026.122457>

Received 13 April 2026; Received in revised form 11 June 2026; Accepted 15 June 2026

Available online 15 June 2026

1359-6454/© 2026 The Authors. Published by Elsevier Inc. on behalf of Acta Materialia Inc. This is an open access article under the CC BY license (<http://creativecommons.org/licenses/by/4.0/>).

diffusion potentially introduces an additional energy barrier when dislocations attempt to overcome intrinsic obstacles originally present in the material, such as substitutional alloying elements. Owing to this short-range, diffusion-mediated interaction, H-induced strengthening predominantly manifests as an increase in the thermally activatable component of the flow stress with a trivial change in the long-range internal stress [18,19]. Consequently, when the available time for deformation is extended, the flow stress contribution arising from H-related activation barrier is progressively relaxed. A typical macroscopic manifestation of this behavior is the enhanced stress relaxation observed when the crosshead of the testing machine is held fixed [17,19,26].

The above findings have collectively provided critical insights into the long-standing debate concerning the interaction mechanisms between diffusible H and dislocations in FCC metals and alloys [7,26–34]. Nevertheless, it remains unclear how this interaction scheme evolves as the temperature is lowered and the H diffusivity is progressively reduced. Under such a circumstance, the coordinated migration of H atoms with moving dislocations is expected to become increasingly infeasible [24,35], whereas solute atoms including H can accumulate more densely in quasi-equilibrated atmospheres around stationary dislocations [23,36,37]. If H atmospheres are allowed to form during the residence time of mobile dislocations at obstacles, dislocation-pinning and the subsequent onset of dynamic strain-aging (DSA) phenomena are accordingly anticipated. Indeed, serrated yielding and the Portevin–Le Chatelier (PLC) effect have been reported in H-charged Ni [27,38,39] and Ni-alloys [40] within a temperature range of 190–230 K. Static strain-aging experiments on these material systems further revealed a pronounced yield point upon reloading [29,30]. This is attributable to H-induced dislocation-pinning, although such strong H–dislocation interactions have sometimes been interpreted in terms of nano-hydride precipitation in dislocation cores [39–42]. However, in Fe–Cr–Ni alloys, the influence of H on dislocation mobility at sub-ambient temperatures remains far less understood, despite the technical importance of 300-series austenitic stainless steels for the practical application to H-related energy facilities [43,44]. Exploring this unforeknown regime is expected to broaden our understanding of H–dislocation interaction mechanisms, encompassing both regimes of high and limited H diffusivity.

In the present study, we address this unresolved issue using the same alloy system consistently examined in our previous works [17–19,45,46]—Fe–24Cr–19Ni (Type310S). Specimens uniformly pre-charged with 8500 at. ppm H were subjected to stress relaxation tests at 213–295 K, during which the temperature- and time-dependent deformation rates, as well as the yielding behavior upon reloading, were systematically evaluated. The results demonstrate that H-induced strain-aging becomes increasingly pronounced with decreasing temperature, revealing a mode of obstructing dislocation motion that is fundamentally different from that operative under ambient conditions.

2. Experimental methodology

2.1. Material and specimen

A hot-rolled rod ($\phi 20$ mm) of a commercial-grade Type310S (Fe–24Cr–19Ni-based) austenitic steel was used in this study. The rod was solution-treated at 1353 K for 600 s, followed by water quenching, resulting in grain sizes of 30–70 μm range (see Appendix). Cylindrical tensile specimens with a gauge diameter of $\phi 4$ mm and a gauge length of 30 mm were machined from the center of the rod. The gauge surfaces were mirror-polished using a 1 μm diamond suspension. Further details of the material, including its chemical composition and the specimen geometry, are provided in [18,19].

2.2. Hydrogen-charging and concentration

Tensile specimens were pre-charged with solute H by exposure to high-purity (99.999%) H_2 gas at 100 MPa and 543 K for >130 h in an autoclave. It should be noted that thermal exposure at this temperature does not induce any changes in microstructure and mechanical behavior of the present steel, even for holding times up to 200 h [18].

After mechanical testing, cylindrical samples with a length of 4 mm were extracted from the gauge sections of the deformed specimens. The residual H concentration was measured by thermal desorption analysis (TDA) using a quadrupole mass spectrometer (HTDS-004, R-DEC, Japan). The measurements were conducted under a constant heating rate of 100 K/h over a temperature range of 298–1073 K. H-charging at 100 MPa resulted in an H concentration of 8500 at. ppm (156 mass ppm), which was significantly higher than the baseline concentration of approximately 200 at. ppm (3.3 mass ppm) in the non-charged specimen.

Based on the literature data of H diffusion coefficient in 300-series austenitic stainless steels at 543 K [47–49], a charging duration of >130 h is sufficient to achieve an almost uniform H distribution throughout the gauge section of the $\phi 4$ mm specimen. Further detail of the confirmation of H saturation is provided in Appendix A1.

2.3. Mechanical tests

Stress relaxation tests were conducted in a stepwise manner during tensile deformation for both non- and H-charged specimens at four temperatures, T : 213, 233, 253, and 295 K (i.e., -60 , -40 , -20 , and 22°C). After deforming the specimen to a predetermined strain level at a constant displacement rate of 0.003 mm/s (corresponding to a nominal strain rate of $10^{-4}/\text{s}$), the machine crosshead was held fixed for 100 s, followed by further extension to the next target strain. Such crosshead-holdings were inserted at nominal strain intervals of 2%. In general, strain-aging characteristics are investigated by statically unloading the specimen for various time durations [29,50–53]. In contrast, an advantage of stress relaxation lies in its ability to continuously capture the material response through uninterrupted monitoring of the stress and strain-rate evolution. For reference, monotonic tensile tests without intermediate stress relaxation were also performed at the same extension rate and temperatures.

In addition to the single stress relaxation tests conducted at given strain levels, repeated stress relaxation tests [12,54] were also carried out at 213 K. The initial loading procedure was identical to that of the single relaxation tests until the crosshead was stopped at a predetermined strain. In the repeated relaxation tests, however, the duration of each relaxation segment was reduced to 10 s. After each 10 s relaxation, the load was reverted to the value at the onset of relaxation, immediately followed by the next relaxation segment for 10 s. This sequence of alternating crosshead-holding and load reversion was repeated ten times, resulting in a total relaxation time of 100 s. The primary objective of these complementary tests was to investigate the time-dependence of relaxation behavior under a fixed reference stress and to quantify the exhaustion rate of mobile dislocations, as discussed later in Section 4.2.3.

A screw-driven electromechanical testing machine (Shimadzu AGX-V2) with a load capacity of 20 kN was used for all mechanical tests described above. Sub-ambient temperature-control was achieved using a thermostatic chamber (Shimadzu TCE-N300A), in which vaporized liquid nitrogen was employed as a refrigerant. During the tests, temperature fluctuations were maintained within ± 1 K. For stress relaxation measurements, thermo-mechanical stability of the specimen–machine assembly is particularly critical to ensure the reliability of the measured stress–time response. Therefore, after the temperature monitored by a thermocouple positioned close to the specimen reached the target value, the system was held for at least 3000 s to allow thermal contraction of the machine pull-rods to fully stabilize before the start of testing. The

tensile strain of the specimen gauge section was directly measured using a contact-type extensometer with an initial gauge length of 25 mm.

In the present study, the experiment under each testing condition was performed using only a single specimen. Nevertheless, as described later, the precise agreement in the stress–strain responses between the monotonic tensile and the stress relaxation tests, together with the fact that the trends of H-effects appeared similarly at multiple strain levels, indicates that the key findings of this study are highly reproducible.

3. Results

3.1. Stress-strain curves during tensile and stress relaxation tests

In Fig. 1, true stress, σ_t –true strain, ϵ_t curves obtained from single stress relaxation tests (solid lines) and monotonic tensile tests (dashed lines) at four different temperatures are shown. The downward spikes observed on the solid σ_t – ϵ_t curves correspond to periods of crosshead-holding during which stress relaxation was performed. At all testing temperatures, the H-charged specimens exhibited higher flow stresses than the non-charged specimens by approximately 40–70 MPa, a strengthening magnitude that is in good agreement with our previous studies [8,18,20]. The overall σ_t – ϵ_t responses were essentially identical between the stress relaxation and monotonic tensile tests, and difficult

to distinguish them.

However, a distinct behavior was observed in the H-charged specimens tested at 213 and 233 K after the stress relaxation stage. Specifically, sharp yield points appeared upon reloading, followed by a reversion of the flow stress to values close to those attained just before crosshead was stopped. Furthermore, in particular strain range, these yield points were accompanied by subsequent serrated flow (*i.e.*, PLC effect) under constant extension rate (see insets in Fig. 1(c) and (d)), a feature that was not observed in the corresponding monotonic tensile tests.

As representative examples, Fig. 2 highlights the reloading-induced yield point behavior around an imposed true strain of 0.02. The magnitude of the stress increase at the yield point—defined as the difference between the local maximum stress upon reloading and the flow stress immediately prior to crosshead holding—was denoted as $\Delta\sigma_{YP}$ and is summarized in Fig. 3 as a function of true strain. In the H-charged specimens, $\Delta\sigma_{YP}$ reached values as high as approximately 20 MPa at 213 K and decreased monotonically with increasing deformation temperature toward 295 K. A similar increase in the reloading yield stress was also weakly observed in the non-charged specimens (Fig. 2(a)); however, the profile of the reloading yield point was considerably more rounded, and its magnitude showed no discernible dependence on temperature (Fig. 3). The origin of this weak yield point in the non-

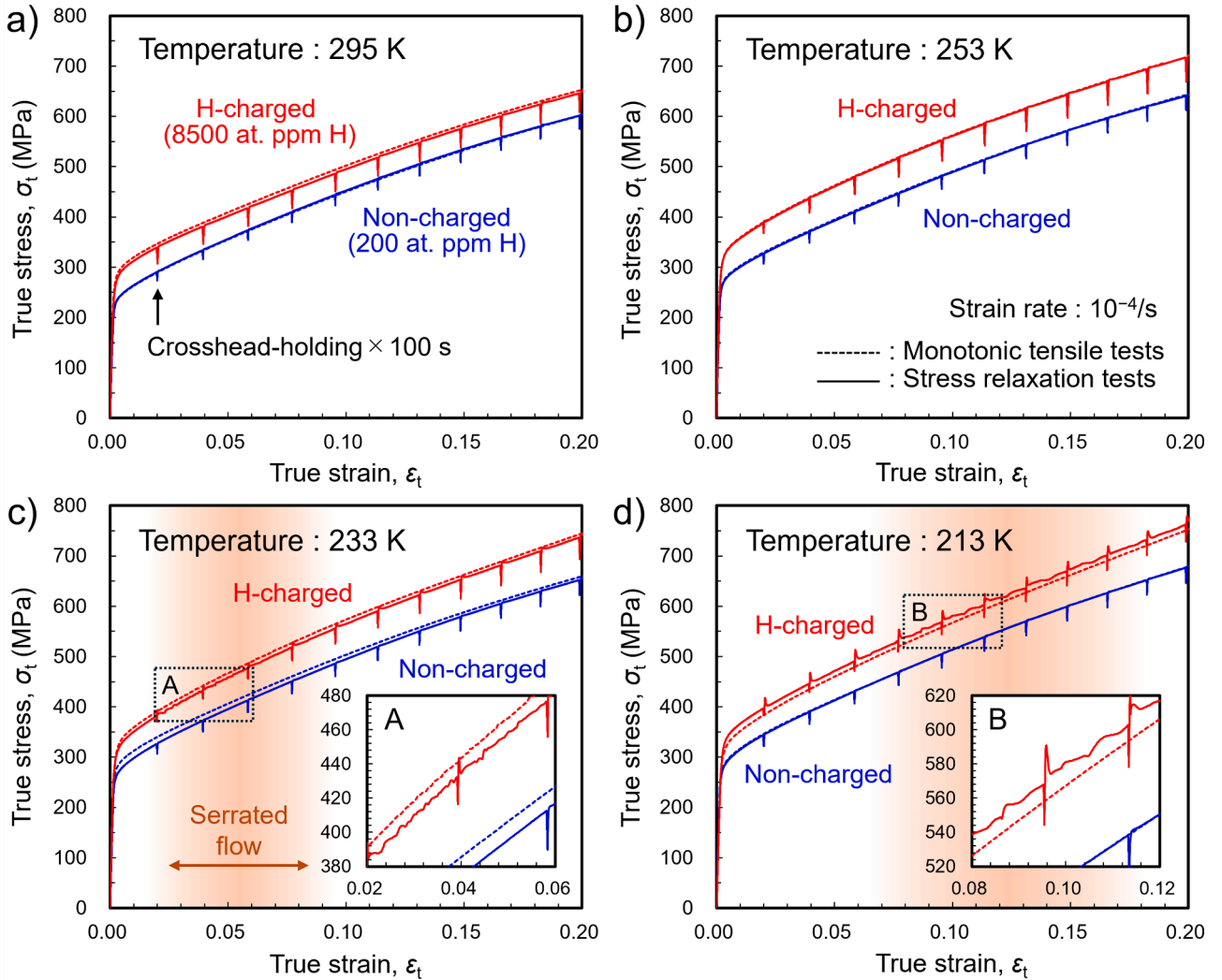


Fig. 1. True stress–true strain curves of non-charged (blue) and H-charged (red) specimens in monotonic tensile tests (dashed lines) and stress relaxation tests (solid lines) at (a) 295 K, (b) 253 K, (c) 233 K, and (d) 213 K. The insets in (c) and (d) magnify the domains surrounded by dashed rectangles A and B, respectively. The shaded regimes in (c) and (d) indicate the strain range where serrated flow appeared in stress relaxation tests.

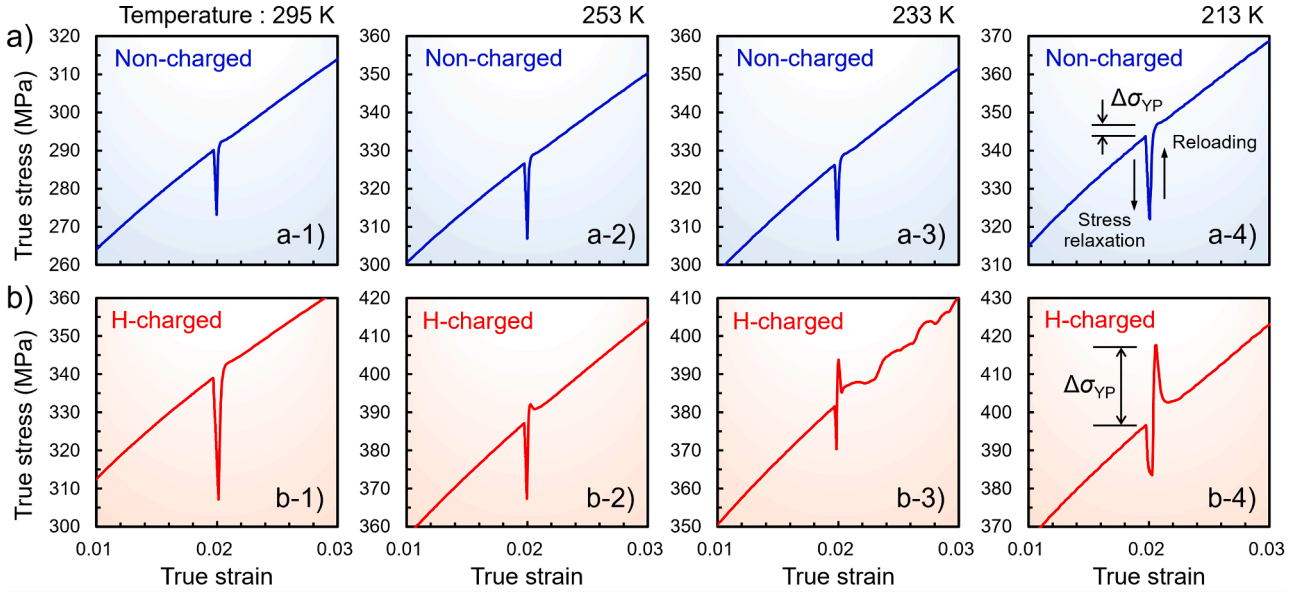


Fig. 2. Magnifications of true stress-true strain curves of (a) non-charged and (b) H-charged specimens (cf. Fig. 1) around the crosshead-holding and reloading periods in stress relaxation tests at a true strain of 0.02. The corresponding deformation temperatures were (a-1)(b-1) 295 K, (a-2)(b-2) 253 K, (a-3)(b-3) 233 K, and (a-4)(b-4) 213 K.

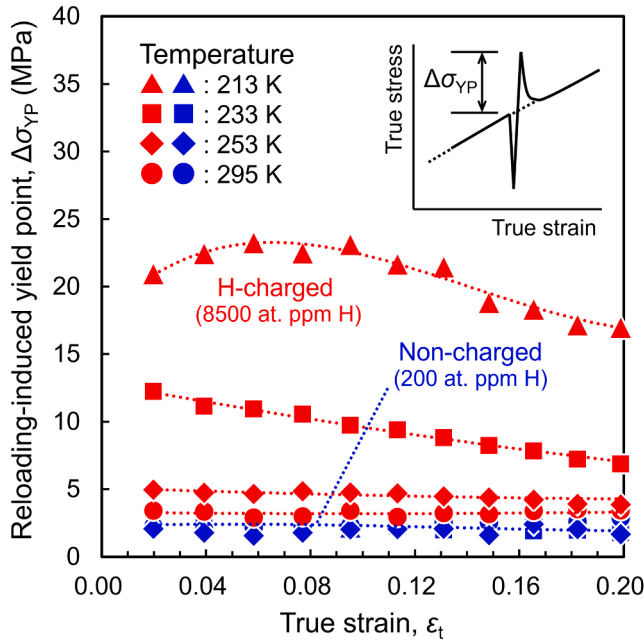


Fig. 3. Magnitudes of the reloading-induced yield point, $\Delta\sigma_{YP}$, at four different temperatures as a function of true strain. The method to determine $\Delta\sigma_{YP}$ is schematically shown on the upper right corner.

charged specimen will be discussed in Section 4.2.3.

3.2. Temperature-effects on stress relaxation behavior

Consistent with the reloading-induced yield point behavior (Fig. 2 and Fig. 3), the stress relaxation response of the H-charged specimens also exhibited a pronounced temperature dependence. Fig. 4 presents the stress drop, $\Delta\sigma$, as a function of logarithmic time during the crosshead-holding periods at three representative true strain levels of 0.020, 0.058, and 0.095 (corresponding to nominal strain, ϵ_n , of 2, 6, and 10%). For clarity, the stress at the onset of each relaxation segment

was set to $\Delta\sigma = 0$ on the vertical axis in Fig. 4, and the subsequent stress drop is represented as a negative quantity. The absolute values of the true stress at the onset of relaxation for the non- and H-charged specimens are indicated separately as σ_{FN} and σ_{FH} , respectively.

After a short initial transient period, the stress relaxation curves of the non-charged specimens exhibited a linear dependence on the logarithm of time under all temperature and strain conditions examined. Such logarithmic time dependence is a characteristic feature of stress relaxation in most metallic materials, where the relaxation behavior is fully ascribed to the thermally activated motion of dislocations [12]. In the H-charged specimens tested at 295 K (Fig. 4(a)), both $\Delta\sigma$ and the rate of stress relaxation were consistently greater than those of the non-charged specimens, reflecting the condition $\sigma_{FH} > \sigma_{FN}$, while still preserving the logarithmic time law. These observations are in good agreement with our previous studies [17,19] and can be interpreted as the time-dependent relaxation of the H-induced effective stress component.

Even though the condition $\sigma_{FH} > \sigma_{FN}$ also held at 213 K, the stress relaxation behavior of the H-charged specimen at this low temperature (Fig. 4(d)) was entirely different from that observed at 295 K. During the initial few seconds, the H-charged specimen followed a relaxation curve similar to that of the non-charged one. Subsequently, the relaxation curve began to deviate upward at a holding time of approximately 10 s. Beyond this point, both $\Delta\sigma$ and the stress relaxation rate became progressively smaller than those in the non-charged condition, indicating that time-dependent plastic deformation is markedly suppressed by solute H. At the intermediate temperatures of 253 and 233 K (Fig. 4(b) and (c)), the relaxation curves exhibited features in which the characteristics at 295 and 213 K were intricately combined. Accordingly, here we primarily focus on the two extreme cases—the contrasting behaviors at 295 and 213 K. The competitive nature of the relaxation processes at intermediate temperatures will be addressed in our forthcoming work.

Stress relaxation is a process in which the elastic strain stored in the specimen-machine assembly is progressively converted into plastic strain occurring within the gauge section of the specimen [12,55,56]. Based on this physical picture, the plastic strain rate during relaxation, $\dot{\epsilon}$, can be estimated using $\dot{\epsilon} = -\dot{\sigma}/E$ where $\dot{\sigma}$ denotes the rate of stress drop (negative quantity) and E is the elastic modulus of specimen-machine system. In Fig. 5, $\dot{\epsilon}$ in non- and H-charged specimens at 295 and 213 K was calculated by time-differentiating the stress relaxation curves

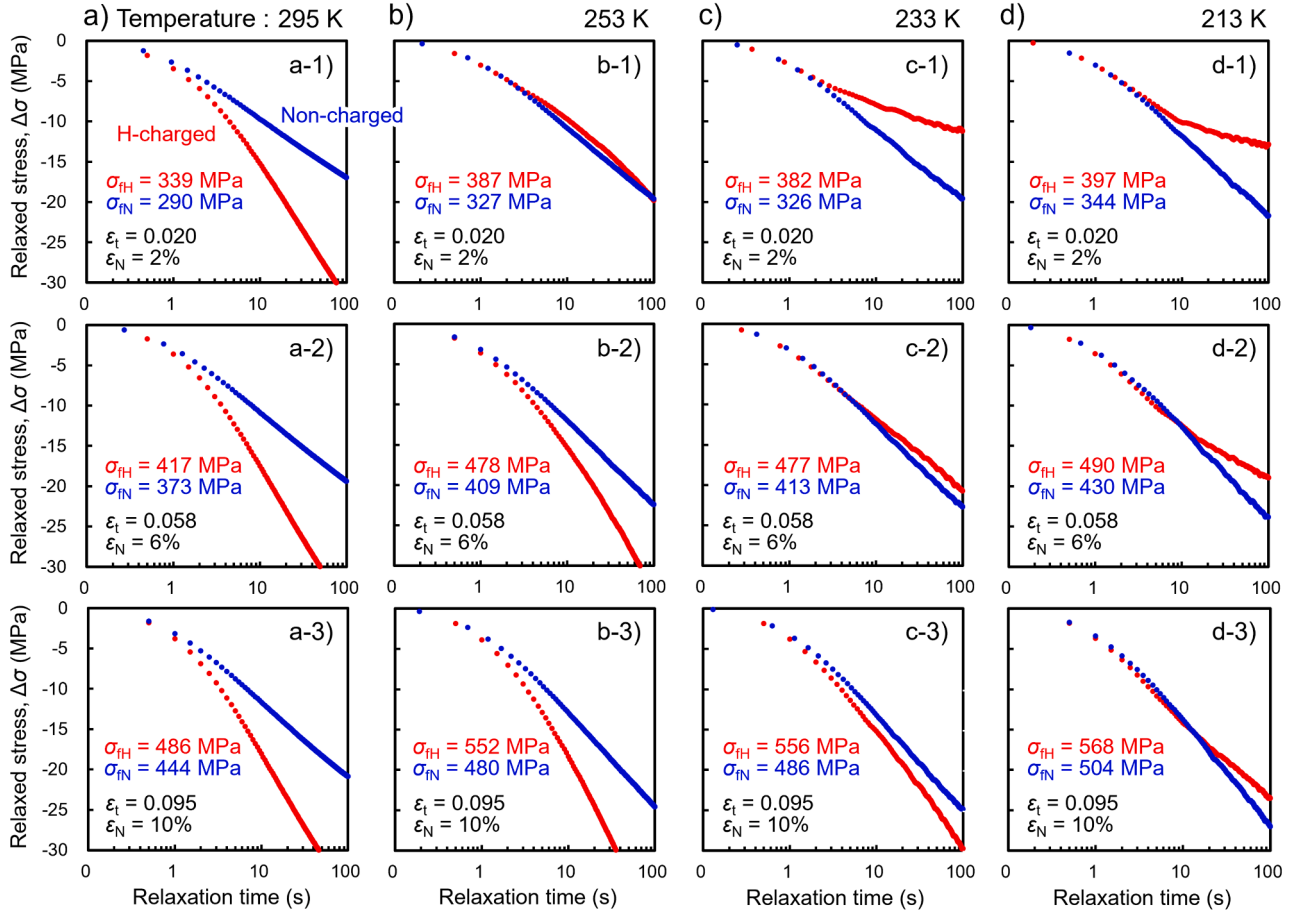


Fig. 4. Stress relaxation curves of non-charged (blue) and H-charged (red) specimens under (a) 295 K, (b) 253 K, (c) 233 K, and (d) 213 K at three representative strain levels. Note that the stress at the onset of each relaxation segment was set to $\Delta\sigma = 0$ for clarity. Refer to σ_{tN} and σ_{tH} in each diagram for the absolute values of flow stress in non- and H-charged specimens at the start of their stress relaxation periods.

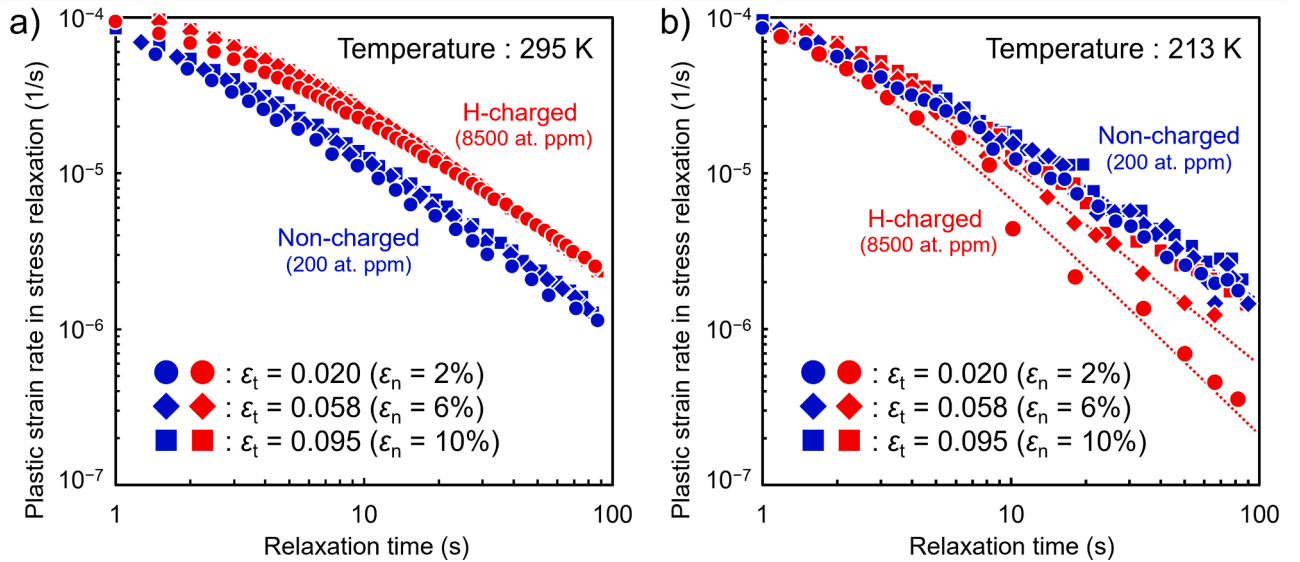


Fig. 5. Plastic strain rate, $\dot{\epsilon}$, during the stress relaxation phases in non- and H-charged specimens, estimated by the relation $\dot{\epsilon} = -\dot{\sigma}/E$, under (a) 295 K and (b) 213 K at three representative strain levels.

shown in Fig. 4(a) and (d). In all cases, the relaxation process started from $\dot{\epsilon} \approx 10^{-4}$ /s, which is identical to the strain rate applied immediately prior to relaxation. This consistency substantiates the sufficient

accuracy of estimating $\dot{\epsilon}$ using $\dot{\epsilon} = -\dot{\sigma}/E$, in view of the continuity of deformation before and after crosshead-holding [12]. Over the course of the 100 s relaxation, the plastic strain rate decreased to the order of

10^{-6} /s or lower. As anticipated from Fig. 4, $\dot{\epsilon}$ in the H-charged specimen was higher than that in the non-charged specimen at 295 K, whereas this trend was reversed at 213 K.

3.3. Decay of deformation rates in repeated stress relaxation

A single stress relaxation test with a holding time of 100 s allows H to interact quasi-statically with mobile dislocations, whose velocity progressively decreases particularly in the later stage of relaxation. However, the interpretation of such behavior remains complex because the applied stress continuously decays during relaxation, resulting in a gradual change in the driving force for dislocation motion. In this context, evaluating the deformation kinetics after restoring the original stress—by performing repeated stress relaxation tests—offers a key advantage.

Fig. 6(a) presents the σ_t - ϵ_t curves obtained during the repeated stress relaxation tests at 213 K up to $\epsilon_t = 0.1$. The data enclosed by the dashed rectangles were extracted as representative examples, and the corresponding cyclic stress relaxation curves for the first six cycles out of ten are reproduced in Fig. 6(b) as a function of time. In the non-charged specimen, $\Delta\sigma$ over a 10 s holding only slightly decreased with increasing relaxation cycle number. In contrast, the H-charged specimen exhibited a remarkable reduction in $\Delta\sigma$ between the first and second relaxations (i.e., during the first 10 s), followed by progressively smaller $\Delta\sigma$ in the third and subsequent cycles. Upon reloading after the relaxation of 100 s in a total, sharp yield point was reproducibly observed (Fig. 6(a)) in the H-charged specimen as for the single relaxation test (Fig. 1(d)).

The uppermost segment of each 10 s relaxation data, including the examples shown in Fig. 6(b), was time-differentiated and defined as the n th initial relaxation rate, $\dot{\sigma}_{in}$, where the subscript n denotes the relaxation cycle number. For each set of repeated relaxation, $\dot{\sigma}_{in}$ was normalized by $\dot{\sigma}_{i1}$ (i.e., the initial relaxation rate in the first cycle) and plotted against relaxation time in Fig. 7(a). An increasing relaxation cycle number gradually decreased $\dot{\sigma}_{in}/\dot{\sigma}_{i1}$ in the non-charged specimen down to ≈ 0.6 . On the other hand, only a few relaxation cycles markedly reduced $\dot{\sigma}_{in}/\dot{\sigma}_{i1}$ in the H-charged specimen to values below 0.2. The reduction rate was, no less, the largest during the first 10 s.

4. Discussion

Our experimental framework revealed a temperature-dependent duality in the role of H in dislocation motion, governed by its diffusivity. At ambient temperature, the strengthening effect of H is fully relaxed with the aid of time, whereas at sub-ambient temperatures the trend was opposite: *H-induced strengthening* (i.e., *dislocation-obstruction*) progressively grows with time. This manifested as suppressed stress relaxation (Fig. 4) and the appearance of a pronounced yield point upon reloading (Fig. 2). In the following, we rationalize this time-dependent obstruction and deformation transient in terms of H mobility in the lattice, the ensuing formation of H atmospheres around dislocations, and resultant pinning of mobile dislocations. These surmises are validated by classical kinetic predictions from the continuum dislocation theory.

The description below focuses exclusively on edge dislocations, whose interactions with solute atoms are expected to be stronger than those of screw counterparts [15,23]. Although the dissociation of an edge dislocation into two Shockley partials and the associated stacking fault is not considered here, similar simplifications have successfully accounted for H-related deformation behavior in the same alloy at ambient temperature [8]. Dislocation dissociation is, in principle, more likely at lower temperatures owing to the reduction in stacking fault energy in Fe-Cr-Ni system [57]. Nevertheless, our recent neutron diffraction experiments on Type310S steel [45] demonstrated that, at least in the temperature range of 200–300 K, a temperature-dependent increase in stacking fault probability becomes discernible only at $\epsilon_t > 0.1$. Accordingly, the following discussion is primarily based on experimental data obtained at $\epsilon_t \leq 0.1$.

4.1. Feasibility of H migration through the lattice

To rationalize the temperature-dependent dislocation-obstruction by solutes, their ability to migrate through the lattice over the experimental time scale must first be considered. Fig. 8 summarizes the temperature-dependence of the diffusion coefficient (Fig. 8(a)), D , and jump frequency (Fig. 8(b)) of H from an octahedral site to its neighbors in Fe-Cr-Ni austenite reported in the literature [47–49], together with the data for C for comparison [58–60]. Experimental diffusion data are available only at elevated temperatures (>400 K for H and >700 K for C). Accordingly, the low-temperature curves in Fig. 8 were obtained by extrapolating the high-temperature data using the reported diffusion

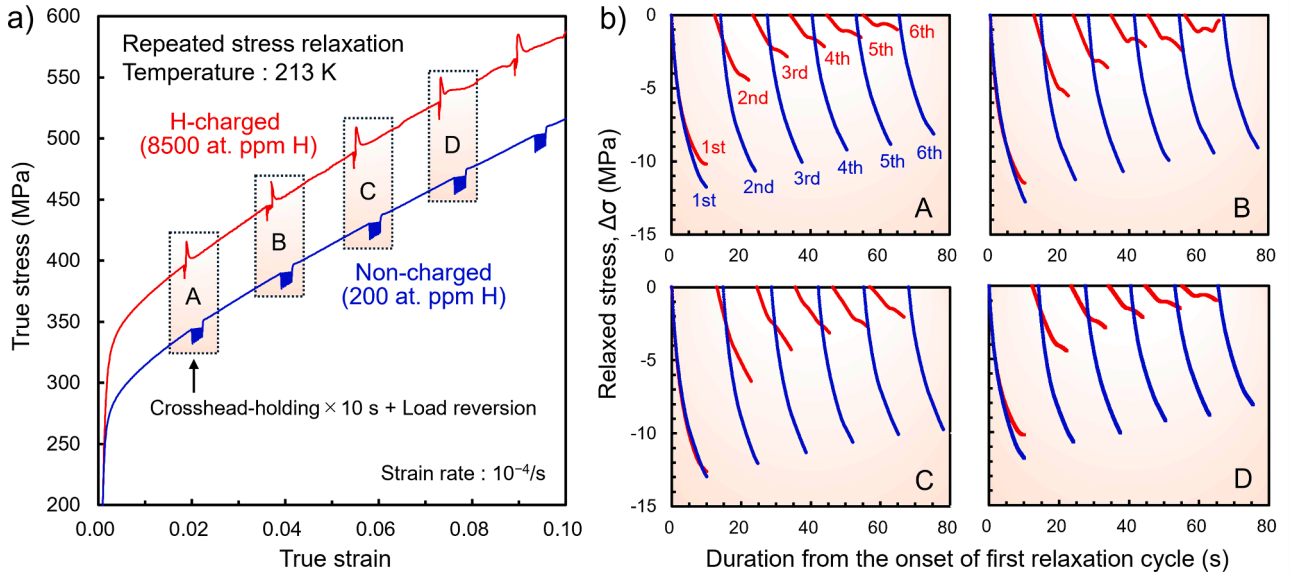


Fig. 6. (a) true stress-true strain curves of non-charged (blue) and H-charged (red) specimens in repeated stress relaxation tests conducted at 213 K. The mechanical responses in the domains surrounded by dashed rectangles A, B, C, and D are extracted and reproduced in (b) as the form of relaxed stress versus time.

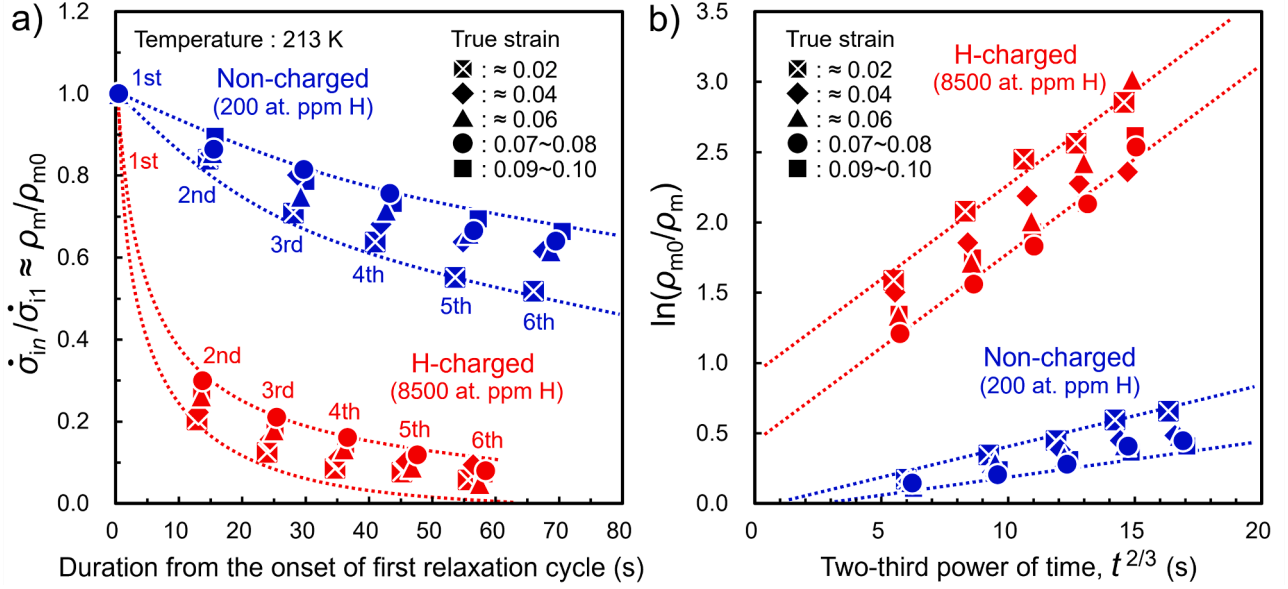


Fig. 7. (a) Ratio of the stress reduction rate (i.e., plastic strain rate) in the beginning of each relaxation cycle, $\dot{\sigma}_{in}$, with respect to that in the first cycle, $\dot{\sigma}_{i1}$, at five different strain levels. $\dot{\sigma}_{in}/\dot{\sigma}_{i1}$ can be approximated as the remaining rate of mobile dislocation density, ρ_m/ρ_{m0} , according to Eq. (5). The logarithms of the inverse of those ρ_m/ρ_{m0} are plotted against the two-thirds power of relaxation time, $t^{2/3}$, in (b) on the basis of Eq. (7).

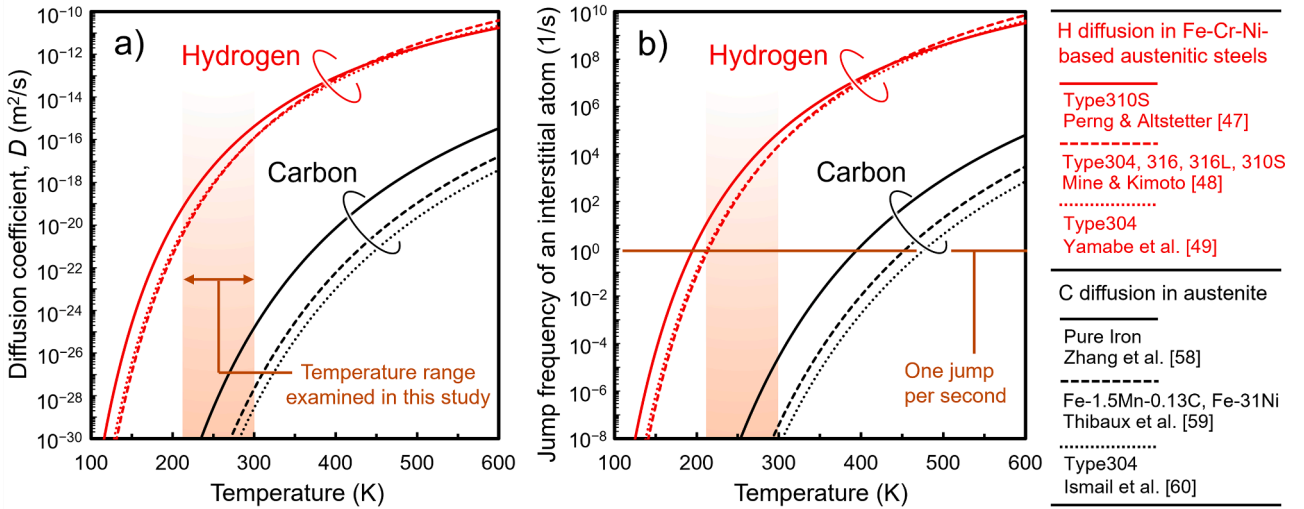


Fig. 8. Temperature-dependencies of (a) diffusion coefficient and (b) jump frequency of solute hydrogen and carbon in austenite, calculated using the diffusion activation parameters for each element provided in the literature [47–49,58–60]. The calculation details are described in [21]. The shaded domain corresponds to the temperature range examined in the present study.

activation parameters. Further details of this calculation are given in [21].

Regarding H, the temperature range examined in the present study (213–295 K; shaded region in Fig. 8) coincides with a sharp decrease in both diffusivity and jump frequency. Whereas H undergoes frequent jumps of $10^4\text{--}10^5/\text{s}$ at 295 K, only one or at most a few jumps are expected at 213 K over a comparable time scale. In this sense, 213 K represents a borderline temperature at which H mobility becomes marginal within a realistic timeframe. This estimate underpins our view that diffusion-mediated interactions between H and dislocations remain the root cause of the time-assisted dislocation-obstruction observed at 213 K. Our prior experiments on the same alloy, in which no H-induced suppression of stress relaxation was observed at 173 K (i.e., the temperature at which H atoms are frozen in the lattice) [8], also support such assertion.

When mapped in terms of diffusivity, the mobility of H at 213 K

corresponds to that of C in austenite at approximately 400–500 K. Notably, diffusion-related dynamic strain aging (DSA) has recently been reported at temperatures slightly above this range in a Fe–Cr–Ni austenitic steel containing a relatively high carbon content (0.2 mass%) deformed at a strain rate of $10^{-4}/\text{s}$ [61]. This correspondence suggests that solute H governs dislocation mobility in a manner essentially analogous to C in austenite, through their diffusion-mediated interactions.

4.2. Formation kinetics of H-dislocation atmosphere

4.2.1. Trapping of mobile dislocations by diffusible H

Given the marginal H diffusivity at 213 K anticipated in Section 4.1, the next step is to assess whether these H can effectively interact with mobile dislocations and trigger DSA. The ability of solute atoms to follow moving dislocations at a constant velocity was recently

quantified by Sills et al. using the following dimensionless parameter, Q [14,15]:

$$Q = \frac{v_d \beta}{4DkT} \quad (1)$$

where v_d is the average velocity of dislocations, k is the Boltzmann constant. β is an elastic size-misfit interaction parameter considering a perfect edge dislocation, defined via shear modulus, $\mu \approx 80$ GPa, Poisson's ratio, $\nu = 0.3$, and the volume expansion per solute atom, $\Delta V (\approx 2.27 \times 10^{-30} \text{ m}^3$ for an H in Type310S steel [46]):

$$\beta = \Delta V \frac{\mu b}{3\pi} \left(\frac{1+\nu}{1-\nu} \right) \quad (2)$$

When a solute atmosphere pre-exists around a dislocation, the dislocation is completely pulled away from the atmosphere when its normalized velocity $Q > 100$. In contrast, for $Q < 0.01$, the atmosphere can fully follow the dislocation motion while maintaining its near-equilibrium distribution. In the intermediate regime between these two extrema, the dislocation experiences a glide resistance arising from the dragging of atmosphere (i.e., solute drag) [16,62], the magnitude of which is maximized around $Q \approx 1$.

Eq. (1) can be further related to the critical strain rates, $\dot{\epsilon}_c$, corresponding to the limits of $Q = 100$, 1, and 0.01 through the well-known Orwain equation:

$$\dot{\epsilon}_c = \frac{4QDkT}{M_T \beta} \rho_m b \quad (3)$$

where $M_T = 3.06$ is the Taylor factor for polycrystalline FCC metals, ρ_m is the mobile dislocation density, and $b = 2.5 \times 10^{-10} \text{ m}$ is the magnitude of Burgers vector. Based on Eq. (3), the temperature-dependence of the three characteristic boundary regimes— $Q = 100$, 1, and 0.01—are parametrically plotted in Fig. 9 using the H diffusivity data provided by Yamabe et al. [49] (Fig. 8(a)). Although direct experimental quantification of ρ_m is challenging, theoretical models have shown that ρ_m rapidly increases to the range of 10^{13} – $10^{14}/\text{m}^2$ immediately after yielding in annealed FCC metals, such as Cu [63] and Type304 austenitic steel [64], then tends to saturate. The $\dot{\epsilon}_c$ corresponding to these realistic ρ_m range for $Q = 100$ (blue), 1 (red), and 0.01 (orange) are delineated by

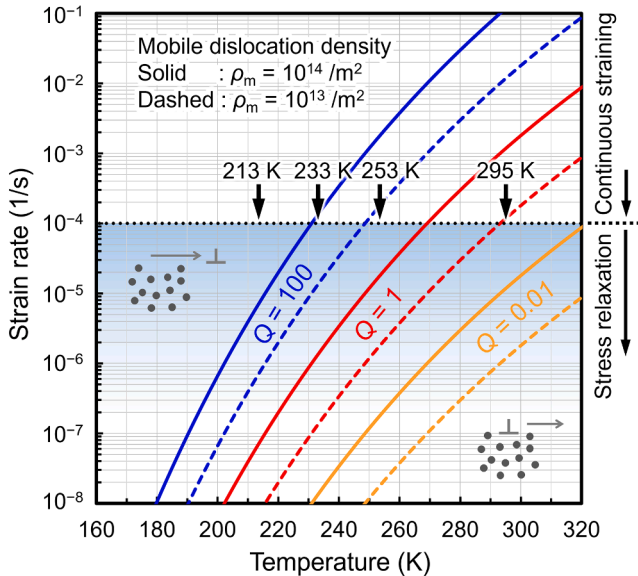


Fig. 9. Temperature-dependence of the critical strain rate corresponding to the limits $Q = 100$, 1, and 0.01 (cf. Eqs. (1) and (3)) for the dynamic interactions of diffusible H with mobile dislocations moving at a steady state velocity. The shaded domain denotes the experimental strain rate range covered by continuous tensile straining and subsequent stress relaxation periods (Fig. 5).

dashed and solid lines in Fig. 9.

The strain rate at the onset of stress relaxation, as well as during continuous tensile straining, was $10^{-4}/\text{s}$ (Fig. 5 and the dotted horizontal line in Fig. 9). Under this condition at 213 K, the deformation state would lie slightly above the $Q = 100$ limit if all dislocations were assumed to move continuously at their average velocity, implying that dynamic H-dislocation interactions are unlikely to be operative prior to crosshead-holding. Once the crosshead was stopped, however, the strain rate promptly decreases to the order of 10^{-6} – $10^{-5}/\text{s}$ or lower (Fig. 5 and the shaded domain in Fig. 9), thereby entering the regime around and below $Q \approx 100$. Moreover, dislocation motion in FCC metals is inherently intermittent rather than strictly continuous, involving periods of arrest at forest dislocations followed by thermally activated release events. Such a stop-go character of dislocation glide has been widely assumed in previous DSA studies [65–68]. Consequently, when a mobile dislocation temporarily ceases its motion at a given location, H atoms that were about to catch up with the moving dislocation, as well as those randomly dispersed in the lattice, can immediately begin to accumulate and form a solute atmosphere. Once the atmosphere starts to form and the resistance to dislocation glide accordingly increases, further development of H atmosphere should become autocatalytic in those trapped dislocations according to the time law described in Section 4.2.2.

4.2.2. Time evolution of dislocation-pinning

The immediate development of an H atmosphere at a temporarily arrested dislocation can be rationalized using the classical kinetic theories of Cottrell atmosphere formation arising from size-misfit interactions with the dislocation strain field [23,36]. By accounting for the drift flux of solute atoms along the gradient of their chemical potential around a dislocation, the following equation was derived by Hartley [53].

$$f = 1 - \exp \left\{ -3N_s b \left(\frac{\pi}{2} \right)^{1/3} \left(\frac{\beta D t}{kT} \right)^{2/3} \right\} \quad (4)$$

In Eq. (4), f denotes the fraction of atmosphere development, with $f = 1$ corresponding to the thermal equilibrium state. N_s is the number of solute atoms in a unit volume, and t denotes time. Given an austenite lattice constant of $\approx 0.36 \text{ nm}$ [9,46] and four octahedral interstitial sites available for H in an FCC unit cell, an H concentration of 8500 at. ppm corresponds to $N_s \approx 7.3 \times 10^{26} \text{ atoms/m}^3$. By substituting this value, the appropriate H diffusion coefficients shown in Fig. 8, and β in Eq. (2) into Eq. (4), the time evolution of the atmosphere fraction f can be obtained, as plotted in Fig. 10 for the four test temperatures employed in the present study.

The characteristic time required for the development of the H Cottrell atmosphere increases progressively with decreasing temperature. Nevertheless, the onset of atmosphere formation occurs within $<1 \text{ s}$ even at 213 K, thereby validating our assertion that H atmosphere formation commences almost immediately once a mobile dislocation is arrested at an obstacle. The evolution of the H atmosphere at 213 K is most pronounced on a time scale of approximately 10 s, as indicated by the dotted vertical line in Fig. 10. Notably, this time scale coincides precisely with the transition at which H-induced suppression of stress relaxation was most clearly discernible (Fig. 4(d) and Fig. 6(b)). Such quantitative agreement between the theoretical kinetics and the experimental trend corroborates the essential role of H Cottrell atmospheres—formed through size-misfit interactions—in obstructing dislocation motion.

It should be noted that, in Fig. 4(d), stress relaxation in the H-charged specimen at 213 K continues appreciably up to an elapsed time of 100 s. This may appear to be inconsistent with the calculation suggesting that dislocation pinning by H atmosphere occurs on the order of several tens of seconds; however, this is not necessarily the case. As the atmosphere develops according to Eq. (4), H in the matrix is progressively depleted, and it is therefore plausible that a certain fraction of

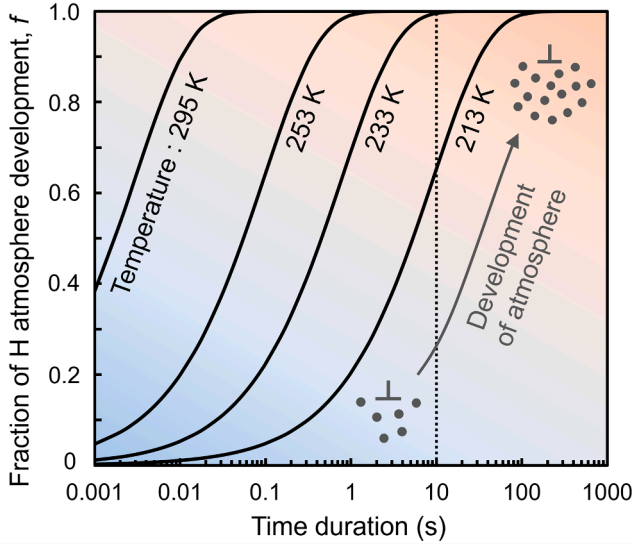


Fig. 10. Time evolution of the H atmosphere around an edge dislocation at four test temperatures examined in this study. The estimation was made by Eq. (4), employing the parameter β defined in Eq. (2). The dotted vertical line delineates a characteristic time of 10 s, at which H-induced suppression of stress relaxation (Fig. 4(d) and Fig. 6(b)) and mobile dislocation exhaustion (Fig. 7(a)) were most pronounced at 213 K.

dislocations remains unpinned and continues to be mobile. This point will be demonstrated in the following section, where the remaining fraction of mobile dislocations is shown not to reach zero even after several tens of seconds. Such an effect is expected to become more pronounced in the high-strain regime, where the dislocation density is higher. Indeed, Fig. 4(d) shows that the stress relaxation rate of the H-charged specimen at longer elapsed times increases with increasing strain. In interpreting this behavior, it should also be kept in mind that H can be collected not only by mobile dislocations but also by forest dislocations.

4.2.3. Exhaustion of mobile dislocations due to the pinning by H atmosphere

In this subsection, we further assess the applicability of Eq. (4) by quantifying the exhaustion rate of mobile dislocations during the crosshead-holding period. During stress relaxation, the mobile dislocation density, ρ_m , naturally decreases as plastic strain accumulates and strain-hardening progresses [12,54]. This manifests as a gradual decay in $\Delta\sigma$ with increasing relaxation cycle number in the repeated stress relaxation tests conducted on the non-charged specimen (Fig. 6(b)). A major part of $\Delta\sigma_{YP}$ (i.e., slight gap between the yield stress upon reloading and the flow stress prior to relaxation) observed in non-charged specimens (Fig. 2(a)) is also attributable to a consequence of strain-hardening during the relaxation [69]. In the H-charged specimen, this intrinsic reduction in ρ_m is superimposed by the progressive pinning of mobile dislocations due to H atmosphere formation, which is expected to make the depletion of mobile dislocations faster.

Meyers et al. proposed a method to evaluate the exhaustion rate of the mobile dislocation density, ρ_m , during stress relaxation events involving strain-aging effects [70]. Taking the time derivative of the Orowan equation, the change in strain rate, $d\dot{\epsilon}$, under a fixed reference stress can be expressed as $d\dot{\epsilon} = M_T(\rho_m b v_d + d\rho_m b v_d)$. If the dislocation velocity, v_d , depends primarily on the applied stress, $d\dot{\epsilon}$ becomes a direct measure of the change in mobile dislocation density, $d\rho_m$, when the stress is held constant. An approximate realization of this condition is achieved in the repeated stress relaxation tests (Fig. 6) by focusing on the plastic strain rate at the onset of each relaxation cycle. Since the plastic strain rate during stress relaxation, $\dot{\epsilon}_{in}$, can be directly converted

into the corresponding stress reduction rate (see Section 3.2), the fraction of ρ_m relative to its initial value at the onset of the first relaxation cycle, ρ_{m0} , can be expressed as follows.

$$\rho_m / \rho_{m0} \approx \dot{\epsilon}_{in} / \dot{\epsilon}_{i1} \approx \dot{\sigma}_{in} / \dot{\sigma}_{i1} \quad (5)$$

From Eq. (5), Fig. 7(a) self-evidently represents the time-dependence of ρ_m / ρ_{m0} at 213 K, wherein its reduction rate in the H-charged specimen was explicitly larger particularly within the first 10 s.

One can assume that the exhaustion of mobile dislocations is proportional to the fraction of H atmosphere development, f (eq. (4)):

$$f = 1 - \exp \left\{ -3N_{sb} \left(\frac{\pi}{2} \right)^{\frac{1}{3}} \left(\frac{A D t}{k T} \right)^{\frac{2}{3}} \right\} \propto \frac{\rho_{m0} - \rho_m}{\rho_{m0}} \quad (6)$$

It follows from Eq. (6) that:

$$\ln(\rho_{m0} / \rho_m) \propto t^{\frac{2}{3}} \quad (7)$$

Fig. 7(b) reproduces the trend observed in Fig. 7(a) on the basis of Eq. (7). In the non-charged specimen, the evolution of $\ln(\rho_{m0} / \rho_m)$ remains relatively small, rendering its detailed time dependence difficult to resolve. In contrast, the H-charged specimen exhibits an approximate proportionality to $t^{2/3}$, providing further support for the consistency between Eq. (4) and the successive pinning of mobile dislocations through the formation of Cottrell atmospheres.

Eq. (5) relies on two essential presumptions [70]: internal stress remains constant throughout the relaxation process; stress-dependence of the velocity of not-yet-pinned dislocations is not changed due to aging. The former is reasonable if one considers that the plastic strain accumulated during stress relaxation is small enough. For the validity of the latter, the testification is made in Appendix A3.

4.3. De-pinning from the H atmosphere

Changes in temperature influence not only the formation kinetics of Cottrell atmospheres but also their spatial extent through the temperature-dependent occupancy of solute atoms at energetically favorable sites [37]. For a positive edge dislocation described in a Cartesian coordinate system, with the dislocation line along the z -axis and the slip plane defined as the x - z plane, the spatial distribution of the solute binding energy, E_B , around the dislocation is given by the following expression [15,23].

$$E_B = \Delta V \frac{\mu b}{3\pi} \left(\frac{1+\nu}{1-\nu} \right) \frac{-y}{x^2 + y^2} = \beta \frac{-y}{x^2 + y^2} \quad (8)$$

Here, an attractive interaction between H and a given site is denoted by positive E_B . By substituting the value of β calculated in Eq. (2), E_B of H atoms is mapped in Fig. 11(a), with the x - and y -axes normalized by the Burgers vector, b . The values of E_B in Fig. 11(a) are expressed in eV using the conversion $1 \text{ J} = 6.24 \times 10^{18} \text{ eV}$. For H in austenitic steels, the binding energy at the dislocation core has been reported to be approximately 0.13 eV [71–73]. The estimated E_B within a region extending $< 2b$ from the dislocation center in Fig. 11(a) is in good agreement with these experimentally [71,72] and computationally [73] determined values.

For a given E_B , the thermal equilibrium occupancy of H and its temperature dependence are generally described by Fermi–Dirac statistics [74]:

$$\frac{C_L}{1 - C_L} = \frac{C_0}{1 - C_0} \exp \left(\frac{E_B}{kT} \right) \quad (9.a)$$

$$C_L = \frac{1}{1 + \frac{1 - C_0}{C_0} \exp \left(-\frac{E_B}{kT} \right)} \quad (9.b)$$

where C_L is the local H concentration at the segregation site, C_0 is the

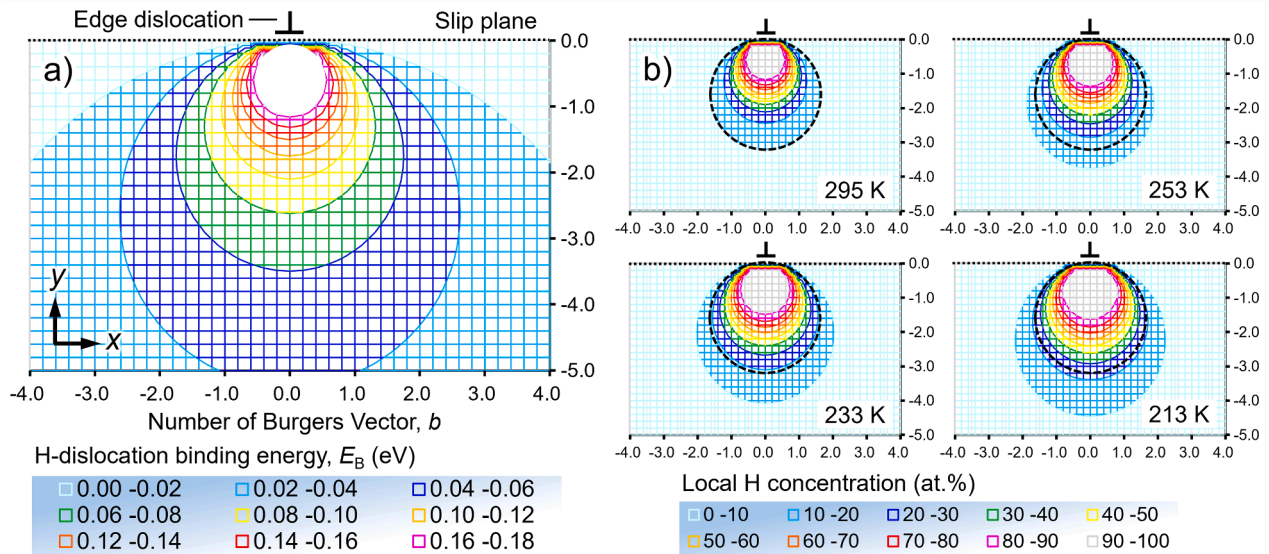


Fig. 11. (a) distribution of H-dislocation binding energy, E_B , around a perfect edge dislocation, calculated based on the size-misfit interactions defined by Eq. (8). The resultant concentration and extent of the H atmosphere according to the Fermi-Dirac statistics (i.e., Eqs. 9.a and 9.b) at four temperatures are shown in (b). The dashed black circles in (b) trace the extent of H atmosphere at 295 K.

background concentration of H in the lattice. Using $C_0 = 8500$ at. ppm (0.85 at.%) and the distribution of E_B shown in Fig. 11(a), the spatial distributions of the local H concentration C_L at the four test temperatures examined in the present study were obtained, as shown in Fig. 11(b). The absolute values of C_L in Fig. 11(b) may be overestimated, since Eqs. 9.a and 9.b do not account for the finite number of available H dissolution sites away from the dislocation center. Nevertheless, the calculations reliably capture the trend of temperature-dependent evolution of the C_L distribution. In particular, decreasing temperature not only enhances the local accumulation of H within the atmosphere but also broadens its spatial extent around the dislocation. Given that a nearly equilibrated H atmosphere develops during 100 s of stress relaxation (Fig. 10), the pronounced yield point observed upon reloading (Fig. 2) can be attributed to the additional stress required to reinitiate the motion of those H-decorated dislocations, i.e., their breakaway from the atmosphere. At intermediate temperatures above 213 K, the dislocations do not completely breakaway from the atmosphere but instead drag it along during glide [14,15] (see also Section 4.2.1). Nevertheless, even under such conditions, a temporal rise in stress is necessary to accelerate the dislocations from a stationary bound state to their steady-state velocity [14], thereby giving rise to the observed yield-point phenomenon.

The temporarily large stress required to accelerate the stationary dislocation increases its magnitude as the eventual steady state solute-dislocation interaction shifts from an atmosphere-drag to a breakaway regime [14], i.e., as Q parameter defined in Eq. (1) increases. Thus, the appearance of more pronounced yield point with lowering the temperature (Fig. 2 and Fig. 3) appears to be a natural consequence. Moreover, since breakaway (or de-pinning) from a solute atmosphere is generally a thermally activated process [23,37,75,76], lowering the temperature further amplifies the required external stress owing to the reduced assistance from atomic thermal vibrations. Barnett et al. emphasized that both the spatial extent of the atmosphere and the solute concentration within it play significant roles in controlling the magnitude of the breakaway stress [37]. Because the total solute-dislocation binding force is determined by integrating the interactions between a dislocation and all individual solute atoms constituting the atmosphere, a denser and more spatially extended atmosphere can more effectively pin the dislocation.

Ultimately, the essential pieces can be distilled into the following three key factors: (I) reduced atmosphere mobility; (II) diminished thermal activation; and (III) an increased concentration and spatial

extent of the atmosphere. The synergy of these factors should have led to a progressively intensified yield point with decreasing temperature (Fig. 2).

4.4. Other related phenomena

Although the foregoing discussion successfully rationalizes both the suppression of stress relaxation and the emergence of yield point upon reloading in H-charged specimens at sub-ambient temperatures, several related characteristic phenomena remain to be quantitatively addressed. A representative example is the PLC effect observed during subsequent continuous plastic flow following the crosshead-holding phases (Fig. 1). At a nominal strain rate of 10^{-4} /s, serrated stress-strain curve was observed only when crosshead-holding was implemented. This suggests that H-induced strain-aging during the holding period leads to an overall hardening of the material, a process that cannot be fully realized under continuous deformation (cf. Fig. 9). Upon subsequent reloading, such hardening is likely followed by the initiation and propagation of deformation bands across the entire gauge length of the specimen. Indeed, the morphology of the serrated stress-strain curves at 213 K (inset of Fig. 1(d)) closely resembles the so-called Type D serrations defined by Rodriguez [77], which are characterized by alternating stress rises and plateau-like regions associated with Lüders band propagation.

Referring again to Fig. 1(c) and (d), the strain range over which serrated flow is observed shifts toward higher strains with decreasing deformation temperature. Estrin and Kubin developed a theoretical framework to rationalize the critical strains for the onset and termination of the PLC effect, emphasizing the balance between mobile and forest dislocation densities as a governing factor [68]. While the trends observed in Fig. 1(c) and (d) are qualitatively consistent with their predictions, interpretation becomes increasingly complicated in the present case due to the intermittent deformation involving stress relaxation. To further elucidate the conditions and underlying mechanisms of the H-related PLC effect, systematic static tensile tests over a wider range of strain rates will be required in future work.

Another notable feature observed in the present experiments, although not directly related to strain-aging phenomena, is the similarity in the initial $\Delta\sigma$ -time responses between the non-charged and H-charged specimens during the early stage of stress relaxation at low temperatures (e.g., Fig. 4(c) and (d)). This behavior contrasts sharply with that at ambient temperature, where the stress relaxation rate in the

H-charged specimen is consistently higher owing to an enhanced effective (*i.e.*, thermal) stress component [17,19] (Fig. 4(a)). In other words, at low temperatures, H atoms dispersed in the lattice contribute to H-induced strengthening in an essentially athermal manner prior to the onset of dynamic dislocation-pinning, thereby increasing the overall flow stress (*e.g.*, Fig. 1(c) and (d)). Recent first-principles calculations by Moriyama et al. revealed attractive interactions between H and substitutional Cr, suggesting the formation of interstitial-substitutional (*i-s*) complexes at octahedral sites involving Cr atoms in its periphery [78, 79]. Such *i-s* complexes are likely unstable at ambient temperature, undergoing repeated nucleation and dissociation. In contrast, at lower temperatures where H mobility is sufficiently suppressed, these complexes may become stabilized at locations where Cr atoms are stochastically clustered, leading to the formation of H–Cr short-range ordered (SRO) zones that interact athermally with dislocations. Clarifying the role of such athermal hardening mechanisms also remains an important subject, particularly in analogy with the strengthening of austenitic steels by N–Cr SROs [5,80].

5. Conclusions

The kinetic interactions between solute hydrogen (H) and mobile dislocations in Fe–24Cr–19Ni mass% (Type310S) austenitic stainless steel at sub-ambient temperatures were systematically investigated by stress relaxation tests. Experiments were performed over 213–295 K on specimens uniformly pre-charged with 8500 at. ppm H in pressurized gaseous H₂ environment. The results demonstrate that suppressed H diffusivity at lower temperatures fundamentally alters H–dislocation interactions, leading to a deformation behavior entirely distinct from that operative at ambient conditions.

- (1) Upon lowering the temperature to 213 K, where H atoms become only marginally diffusible (*i.e.*, few jumps per second), the presence of solute H markedly suppressed stress relaxation and induced a pronounced yield point upon reloading. The magnitude of this reloading-induced yield-point increased monotonically with decreasing temperature.

- (2) The suppressed stress relaxation at low temperature was attributed to successive pinning of mobile dislocations through the formation of H Cottrell atmospheres. This dynamic strain-aging (DSA) process accelerated the exhaustion rate of mobile dislocations during relaxation, with its kinetics well described by classical dislocation theory based on continuum mechanics.
- (3) The reloading-induced yield point originates from the extra stress required to remobilize dislocations from their H-pinned state. The escalation of yield point at lower temperatures is rationalized by the synergistic effects of (I) reduced mobility of the H atmosphere, (II) diminished thermal activation for dislocation depinning, and (III) increased concentration and spatial extent of the H atmosphere, collectively strengthening the dislocation-pinning force.

Acknowledgement

This work was financially supported by JSPS KAKENHI (Grant No. 24K17180) and promotion from the Iketani Science and Technology Foundation (Grant No. 0371,199-A).

CRediT authorship contribution statement

Yuhei Ogawa: Writing – original draft, Investigation, Funding acquisition, Conceptualization. **Tatsuya Ito:** Writing – review & editing, Conceptualization. **Haruki Nishida:** Writing – review & editing, Conceptualization. **Osamu Takakuwa:** Writing – review & editing, Conceptualization. **Kaneaki Tsuzaki:** Writing – review & editing, Conceptualization. **Stefanus Harjo:** Writing – review & editing, Supervision. **Akinobu Shibata:** Writing – review & editing, Supervision.

Declaration of competing interest

The authors declare that they have no known competing financial interests or personal relationships that could have appeared to influence the work reported in this paper.

Appendix

A1. Progress of hydrogen dissolution during thermal pre-charging

The dissolution of H atoms from the gauge surface of round-bar specimens can be approximated as a two-dimensional diffusion problem in a solid cylinder governed by Fick's law. This classical problem has been solved mathematically by Crank in his textbook [81]. Under the boundary condition that the cylinder surface is instantaneously maintained at a constant (saturated) solute concentration while the internal concentration is initially zero, the generalized solution is given by:

$$\frac{M_t}{M_\infty} = 1 - \sum_{j=1}^{\infty} \frac{4}{\alpha_j^2} \exp\left(-\frac{4D\alpha_j^2 t}{d^2}\right) \quad (\text{A1})$$

where M_t is the total quantity of solute entered into the cylinder at a time duration, t . M_∞ is the corresponding quantity at an infinite time (*i.e.*, quantity at a saturation), d is the diameter of cylinder, and α_j is the roots of the Bessel function of the first kind of zero order with positive integers, j (*i.e.*, $\alpha_1 = 2.4048$, $\alpha_2 = 5.5201$, $\alpha_3 = 8.6537$...). Using the activation parameters for H diffusion in 300-series austenitic stainless steels measured by several researchers [47–49], the H diffusion coefficient at the charging H₂ gas temperature of 543 K is calculated to be $D = 5.7 \times 10^{-12} - 1.0 \times 10^{-11}$ m²/s. Introducing these values into Eq. (A1) and neglecting the higher order terms with $j > 100$, the evolution of H penetration into a specimen with a diameter $d = 4$ mm is derived as shown in Fig. A1.

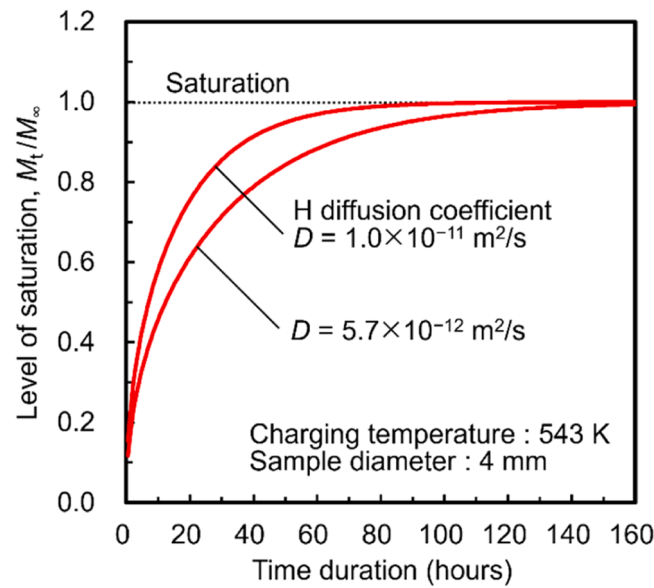


Fig. A1. Time evolution of the H saturation level in a $\phi 4$ mm cylindrical sample during the thermal pre-charging in pressurized H_2 gas at 543 K (cf. Eq. (A1)). The H diffusion coefficients measured in [47–49] were used for calculation.

Referring to Fig. A1, the fraction M_t/M_∞ rapidly increases within the first 50 h during thermal pre-charging, then tend to show its plateau after the passage of 100 h. Thus, the charging duration of >130 h employed in this study was deemed to be long enough to realize macroscopically uniform H distribution within the specimen's gauge part.

A2. Deformation twinning at low temperatures

Our previous studies have shown that Type310S steel exhibits deformation twinning at and below ambient temperature [45,82]. The critical strain for the onset and evolution of twinning decreases monotonically with decreasing temperature, and is further reduced in the presence of solute H [45, 46,82,83]. The emergence of deformation twins is therefore expected to provide an alternative plastic deformation mode when dislocation motion is effectively suppressed by trapping within the H atmosphere. Such twin-mediated plasticity may contribute to the manifestation of the reloading-induced yield point, in conjunction with the dislocation de-trapping events discussed in Section 4.3. Accordingly, the presence or absence of deformation twins within the strain range examined in the present study must be carefully confirmed especially at 213 K.

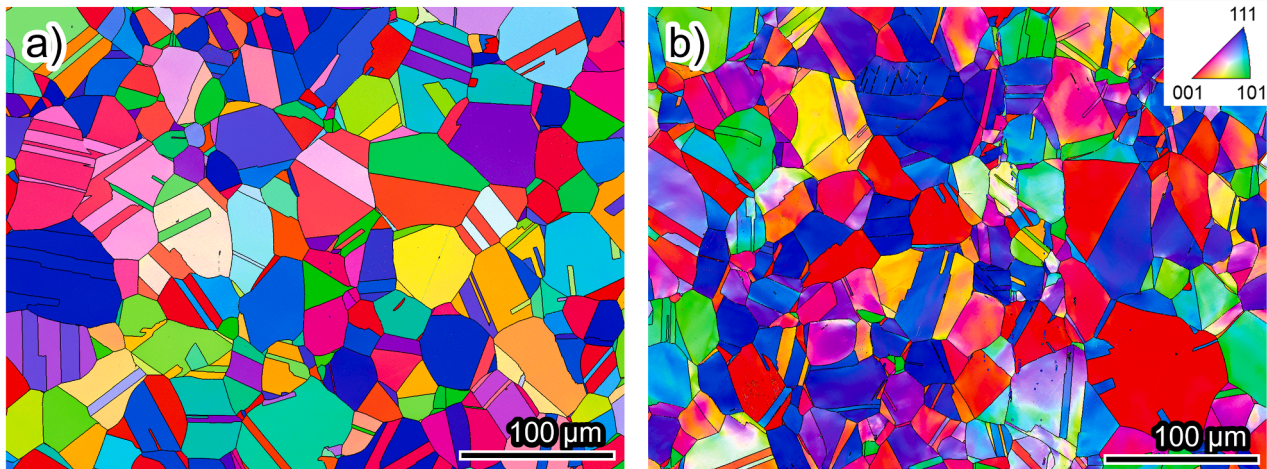


Fig. A2. Inverse pole figure (IPF) maps of the microstructures in (a) pre-deformed sample and (b) H-charged specimen subjected to repeated stress relaxation test (cf. Fig. 6), analyzed by EBSD. In (b), the imposed true strain was approximately 0.1. The color codes indicate the crystal orientation along the tensile axis, which corresponds to the vertical direction in the picture.

Fig. A2(b) presents an electron backscatter diffraction (EBSD) image of the H-charged specimen subjected to the repeated stress-relaxation test shown in Fig. 6, up to a true strain of approximately 0.1. Prior to observation, the specimen was sectioned at its mid-diameter plane parallel to the loading axis and mechanically polished. EBSD measurements were conducted using a field-emission scanning electron microscope (Carl Zeiss Sigma) equipped with a Bruker QUANTAX EBSD system, operated at an acceleration voltage of 20 kV with a step size of 150 nm. As a reference state, an image of the pre-deformed microstructure is also provided in Fig. A2(a).

As revealed by the inverse pole figure (IPF) map along the loading axis, the present Type310S steel initially has randomly oriented austenite grains with their sizes of 30–70 μm range. After being plastically deformed at 213 K, deformation twins were scarcely observed, appearing only in a limited

number of grains most favorably oriented for twinning (*i.e.*, with tensile directions close to $\langle 111 \rangle$ [84]). The density of deformation twins was almost negligible, while a pronounced reloading-induced yield point was clearly observed in this specimen even at strain levels well below 0.1 (Fig. 6(a)). This observation indicates that deformation twinning does not play a significant role in the emergence of the reloading-induced yield point. The phenomenon can therefore be attributed purely to the interaction between dislocations and solute H.

A3. Kinetics of dislocation motion under strain-aging

The interpretation of stress relaxation behavior under strain-aging is rather complex since the changes in mobile dislocation density, their velocity, and obstacle properties possibly affect the relaxation strain rate in a combined manner [12,69,70,85]. In Section 4.2.3, we presumed that the stress-dependence of the velocity of not-yet-pinned dislocations remains unchanged even under the evolution of H-induced aging phenomena. This assumption should be validated somehow in order to substantiate the estimation of mobile dislocation exhaustion rate described in Fig. 7(a).

When dislocations move through thermally activated mechanisms, the flow stress, σ , exhibits a power-law dependence on the strain rate, $\dot{\epsilon}$, as described in the state variable theory proposed by Hart [86].

$$\sigma = \sigma_0 (\dot{\epsilon} / \dot{\epsilon}_0)^m \quad (\text{A2})$$

where σ_0 and $\dot{\epsilon}_0$ are material constants, and m is the strain-rate sensitivity exponent, defined as:

$$m = \frac{\partial \ln \sigma}{\partial \ln \dot{\epsilon}} \quad (\text{A3})$$

By invoking the Orowan equation, $\dot{\epsilon} = M_T \rho_m b v_d$, Eq. (A3) can be rewritten as:

$$\frac{1}{m} = \frac{\partial \ln \dot{\epsilon}}{\partial \ln \sigma} = \frac{\partial \ln \rho_m}{\partial \ln \sigma} + \frac{\partial \ln v_d}{\partial \ln \sigma} = \frac{\partial \ln v_d}{\partial \ln \sigma} \bigg|_{\rho_m} \quad (\text{A4})$$

Thus, when the mobile dislocation density ρ_m remains constant, the strain-rate sensitivity parameter m exclusively reflects the stress dependence of the dislocation velocity v_d . In stress-relaxation tests, the plastic strain rate $\dot{\epsilon}$ exhibits a one-to-one correspondence with the stress-reduction rate $-\dot{\sigma}$ (see Section 3.2). Accordingly, the relevant m value can be determined from a $\ln \sigma - \ln(-\dot{\sigma})$ plot by calculating the slope at any locus.

The m value can therefore serve as an index to validate the assumption of an invariant stress-dependence of the dislocation velocity, which is implicitly adopted in the evaluation of ρ_m / ρ_{m0} in Section 4.2.3. Fig. A3 shows the $\ln \sigma - \ln(-\dot{\sigma})$ plots constructed from the initial portions of each relaxation cycle in the repeated stress-relaxation tests at 213 K, corresponding to the data segments used to determine $\dot{\sigma}_{in}$ in Eq. (5). For clarity, all curves were intentionally offset along $\ln(-\dot{\sigma})$ axis. Since the mobile dislocation density continuously decreases during stress relaxation, the assumption of a constant ρ_m in Eq. (A4) does not strictly hold. However, because the present analysis focuses on the short-time response immediately after the onset of each relaxation step, insignificant variation in ρ_m over the time interval considered here may be a reasonable approximation. As a representative example, the first to third relaxation cycles at a true strain of approximately 0.02 are selectively presented. For cycles beyond the third, the $\ln \sigma - \ln(-\dot{\sigma})$ responses became excessively noisy, rendering the determination of their slopes ambiguous.

In the absence of strain-aging effects, the $\ln \sigma - \ln(-\dot{\sigma})$ responses obtained from repeated stress-relaxation tests in FCC metals and alloys normally trace an identical trajectory [69,87], indicating that the obstacle properties governing the thermally activated deformation process remain unchanged. Such behavior can exactly be seen in Fig. A3(a), where all the $\ln \sigma - \ln(-\dot{\sigma})$ curves exhibit almost an identical slope. Even in the H-charged specimen, similar trend was explicitly identified. A notable point was the coincidence of the $\ln \sigma - \ln(-\dot{\sigma})$ slope between first and second cycles, wherein the evolution of aging was the most remarkable within the beginning 10 s (Fig. 10). This implies that the velocity of still mobile (*i.e.*, not-yet-pinned) dislocations under the given reference stress was unchanged by aging, validating the presumption for estimating ρ_m / ρ_{m0} in Section 4.2.3. An identical trend was confirmed also at other strain level.

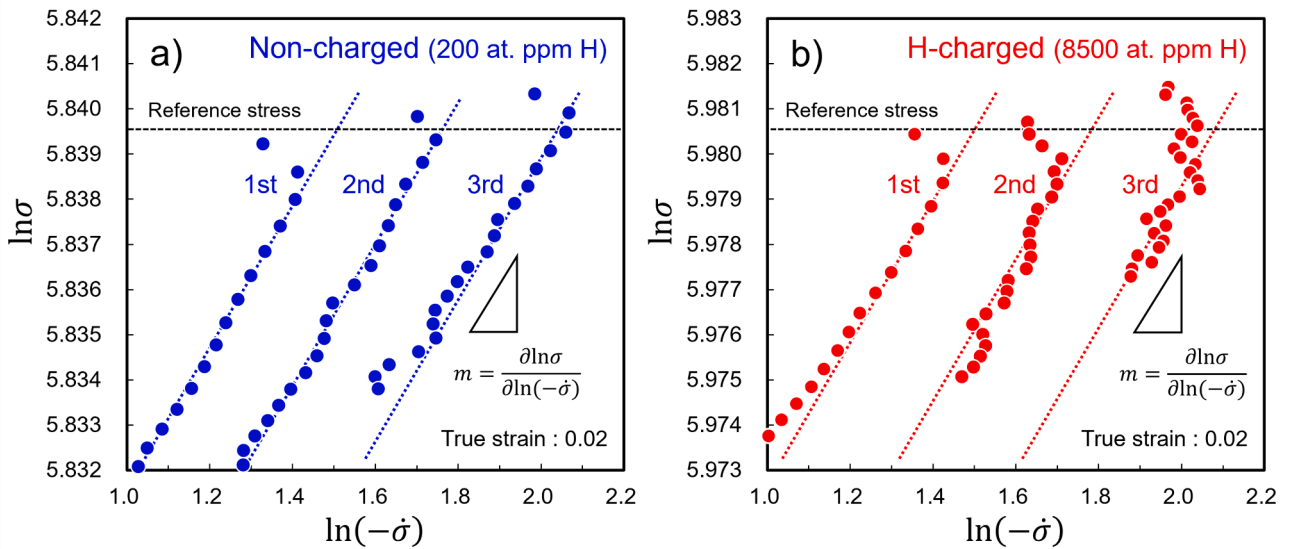


Fig. A3. $\ln \sigma - \ln(-\dot{\sigma})$ plots at beginning of first to third relaxations in repeated stress relaxation tests (Fig. 6) of (a) non-charged and (b) H-charged specimens at temperature of 213 K and a true strain of approximately 0.02. The slope of each curve reflects the strain rate sensitivity, m , defined in Eqs. (A2)-(A4).

References

- [1] P. Marshall, *Austenitic Stainless Steels: Microstructure and Mechanical Properties*, Springer, 1984.
- [2] V.G. Gavriljuk, H. Berns, *High Nitrogen Steels Structure, Properties, Manufacture, Applications*, Springer, 1999.
- [3] Y. Nakada, A.S. Keh, Solid-solution strengthening in Ni-C alloys, *Metall. Trans.* 2 (1971) 441–447, <https://doi.org/10.1007/BF02663332>.
- [4] U.F. Kocks, R.E. Cook, R.A. Mulford, Strain aging and strain hardening in Ni-C alloys, *Acta Metall.* 33 (1985) 623–638, [https://doi.org/10.1016/0001-6160\(85\)90026-4](https://doi.org/10.1016/0001-6160(85)90026-4).
- [5] M.L.G. Byrnes, M. Grujicic, W.S. Owen, Nitrogen strengthening of a stable austenitic stainless steel, *Acta Metall.* 35 (1987) 1853–1862, [https://doi.org/10.1016/0001-6160\(87\)90131-3](https://doi.org/10.1016/0001-6160(87)90131-3).
- [6] L.H. de Almeida, I. Le May, P.R.O. Emygdio, Mechanistic modeling of dynamic strain aging in austenitic stainless steels, *Mater. Charact.* 41 (1998) 137–150, [https://doi.org/10.1016/S1044-5803\(98\)00031-X](https://doi.org/10.1016/S1044-5803(98)00031-X).
- [7] D.P. Abraham, C.J. Altstetter, The effect of hydrogen on the yield and flow stress of an austenitic stainless steel, *Metall. Mater. Trans. A* 26 (1995) 2849–2858, <https://doi.org/10.1007/BF02669643>.
- [8] Y. Ogawa, O. Takakuwa, K. Tsuzaki, Solid-solution hardening by hydrogen in Fe–Cr–Ni-based austenitic steel: temperature and strain rate effects, *Mater. Sci. Eng.: A* 879 (2023) 145281, <https://doi.org/10.1016/j.msea.2023.145281>.
- [9] H.M. Ledbetter, M.W. Austin, Dilatation of an fcc Fe–Cr–Ni alloy by interstitial carbon and nitrogen, *Mater. Sci. Technol.* 3 (1987) 101–104, <https://doi.org/10.1179/mst.1987.3.2.101>.
- [10] N. Ohkubo, K. Miyakusa, Y. Uematsu, H. Kimura, Effect of alloying elements on the mechanical properties of the stable austenitic stainless steel, *ISIJ Int.* 34 (1994) 764–772, <https://doi.org/10.2355/isijinternational.34.764>.
- [11] E.I. Samuel, B.K. Choudhary, K. Bhanu Sankara Rao, Influence of temperature and strain rate on tensile work hardening behaviour of type 316 LN austenitic stainless steel, *Scr. Mater.* 46 (2002) 507–512, [https://doi.org/10.1016/S1359-6462\(02\)00023-4](https://doi.org/10.1016/S1359-6462(02)00023-4).
- [12] D. Caillard, J.L. Martin, *Thermally Activated Mechanisms in Crystal Plasticity*, 1st ed., Pergamon, 2003.
- [13] A.G. Evans, R.D. Rawlings, The thermally activated deformation of crystalline materials, *Phys. Status Solidi(B)* 34 (1969) 9–31, <https://doi.org/10.1002/pssb.19690340102>.
- [14] E.N. Epperly, R.B. Sills, Transient solute drag and strain aging of dislocations, *Acta Mater.* 193 (2020) 182–190, <https://doi.org/10.1016/j.actamat.2020.03.031>.
- [15] R.B. Sills, W. Cai, Solute drag on perfect and extended dislocations, *Philos. Mag.* 96 (2016) 895–921, <https://doi.org/10.1080/14786435.2016.1142677>.
- [16] H. Yoshinaga, S. Morozumi, The solute atmosphere around a moving dislocation and its dragging stress, *Philos. Mag.: J. Theor. Exp. Appl. Phys.* 23 (1971) 1367–1385, <https://doi.org/10.1080/14786437108217008>.
- [17] Y. Ogawa, M. Tanaka, T. Fujita, A. Shibata, Thermally activated dislocation motion in hydrogen-alloyed Fe–Cr–Ni austenitic steel revisited via Haasen plot, *Int. J. Hydrog. Energy* 74 (2024) 170–182, <https://doi.org/10.1016/j.ijhydene.2024.06.113>.
- [18] Y. Ogawa, A. Shibata, Plastic flow in Fe–Cr–Ni austenitic steel under the presence of solute H: a study via room temperature creep, *Acta Mater.* 285 (2025) 120659, <https://doi.org/10.1016/j.actamat.2024.120659>.
- [19] Y. Ogawa, A. Shibata, Refining hydrogen-dislocation interaction model for thermally activated plasticity in Fe–Cr–Ni austenitic steels: analyzing stress-dependent activation volume, *Acta Mater.* 306 (2026) 121896, <https://doi.org/10.1016/j.actamat.2026.121896>.
- [20] Y. Ogawa, T. Fujita, Solid solution-hardening by hydrogen in Fe–Cr–Ni-based austenitic steel studied by strain rate sensitivity measurement: contributions of effective stress and solute drag, *Mater. Sci. Eng.: A* 911 (2024) 146941, <https://doi.org/10.1016/j.msea.2024.146941>.
- [21] Y. Ogawa, O. Takakuwa, J. Moriyama, H. Nishida, K. Tsuzaki, A. Shibata, Phenomenology and mechanisms of hydrogen-Induced solid solution-Hardening in Fe–Cr–Ni austenitic steels, *Mater. Trans.* 67 (2026) 385–404, <https://doi.org/10.2320/matertrans.MT-M2025161>.
- [22] C. Nowak, X.W. Zhou, R.B. Sills, Validating continuum theory for Cottrell atmosphere solute drag by molecular dynamics simulations, *J. Mech. Phys. Solids* 183 (2024) 105514, <https://doi.org/10.1016/j.jmps.2023.105514>.
- [23] P.M. Anderson, J.P. Hirth, J. Lothe, *Theory of Dislocations*, 3rd ed., Cambridge University Press, 2017.
- [24] J. Tien, A.W. Thompson, I.M. Bernstein, R.J. Richards, Hydrogen transport by dislocations, *Metall. Trans. A* 7 (1976) 821–829, <https://doi.org/10.1007/BF02644079>.
- [25] J. Friedel, *Dislocations*, 1st ed., Pergamon Press, 1964.
- [26] D.P. Abraham, C.J. Altstetter, Hydrogen-enhanced localization of plasticity in an austenitic stainless steel, *Metall. Mater. Trans. A* 26 (1995) 2859–2871, <https://doi.org/10.1007/BF02669644>.
- [27] T. Boniszewski, G.C. Smith, The influence of hydrogen on the plastic deformation ductility, and fracture of nickel in tension, *Acta Metall.* 11 (1963) 165–178, [https://doi.org/10.1016/0001-6160\(63\)90209-8](https://doi.org/10.1016/0001-6160(63)90209-8).
- [28] T. Matsumoto, J. Eastman, H.K. Birnbaum, Direct observations of enhanced dislocation mobility due to hydrogen, *Scr. Metall.* 15 (1981) 1033–1037, [https://doi.org/10.1016/0036-9748\(81\)90249-0](https://doi.org/10.1016/0036-9748(81)90249-0).
- [29] G. Girardin, D. Delafosse, Solute-dislocation interactions: modelling and experiments in hydrogenated nickel and nickel base alloys, *Mater. Sci. Eng.: A* 387–389 (2004) 51–54, <https://doi.org/10.1016/j.msea.2004.02.071>.
- [30] G. Girardin, D. Delafosse, Measurement of the saturated dislocation pinning force in hydrogenated nickel and nickel base alloys, *Scr. Mater.* 51 (2004) 1177–1181, <https://doi.org/10.1016/j.scriptamat.2004.07.012>.
- [31] I.M. Robertson, The effect of hydrogen on dislocation dynamics, *Eng. Fract. Mech.* 68 (2001) 671–692, [https://doi.org/10.1016/S0013-7944\(01\)00011-X](https://doi.org/10.1016/S0013-7944(01)00011-X).
- [32] P.J. Ferreira, I.M. Robertson, H.K. Birnbaum, Hydrogen effects on the interaction between dislocations, *Acta Mater.* 46 (1998) 1749–1757, [https://doi.org/10.1016/S1359-6454\(97\)00349-2](https://doi.org/10.1016/S1359-6454(97)00349-2).
- [33] J.P. Chateau, D. Delafosse, T. Magnin, Numerical simulations of hydrogen–dislocation interactions in fcc stainless steels: part I: hydrogen–dislocation interactions in bulk crystals, *Acta Mater.* 50 (2002) 1507–1522, [https://doi.org/10.1016/S1359-6454\(02\)00008-3](https://doi.org/10.1016/S1359-6454(02)00008-3).
- [34] C.W. Tien, C.J. Altstetter, Hydrogen-enhanced plasticity of 310S stainless steel, *Mater. Chem. Phys.* 35 (1993) 58–63, [https://doi.org/10.1016/0254-0584\(93\)90177-N](https://doi.org/10.1016/0254-0584(93)90177-N).
- [35] H.K. Birnbaum, P. Sofronis, Hydrogen-enhanced localized plasticity—A mechanism for hydrogen-related fracture, *Mater. Sci. Eng.: A* 176 (1994) 191–202, [https://doi.org/10.1016/0921-5093\(94\)90975-X](https://doi.org/10.1016/0921-5093(94)90975-X).
- [36] A.H. Cottrell, *Dislocations and Plastic Flow in Crystals*, Oxford Univ. Press, New York, 1953.
- [37] D.M. Barnett, W.C. Oliver, W.D. Nix, The binding force between an edge dislocation and a fermi-dirac solute atmosphere, *Acta Metall.* 30 (1982) 673–678, [https://doi.org/10.1016/0001-6160\(82\)90116-X](https://doi.org/10.1016/0001-6160(82)90116-X).
- [38] B.A. Wilcox, G.C. Smith, The Portevin-Le Chatelier effect in hydrogen charged nickel, *Acta Metall.* 12 (1964) 371–376, [https://doi.org/10.1016/0001-6160\(64\)90006-9](https://doi.org/10.1016/0001-6160(64)90006-9).
- [39] J.S. Blakemore, The Portevin-Le Chatelier effect in hydrogenated nickel, *Metall. Trans.* 1 (1970) 145–149, <https://doi.org/10.1007/BF02819254>.
- [40] J.S. Blakemore, The portevin-le chatelier effect in hydrogenated nickel alloys, *Metall. Mater. Trans.* 1 (1970) 151–156, <https://doi.org/10.1007/BF02819255>.
- [41] G.P.M. Leyson, B. Grabowski, J. Neugebauer, Multiscale description of dislocation induced nano-hydrides, *Acta Mater.* 89 (2015) 50–59, <https://doi.org/10.1016/j.actamat.2015.01.057>.
- [42] F.D. León-Cázarez, X. Zhou, C. Alleman, C.S. Marchi, Dislocation nano-hydrides in nickel: nucleation, evolution and effects on dislocation behaviors, *J. Mech. Phys. Solids* 205 (2025) 106310, <https://doi.org/10.1016/j.jmps.2025.106310>.
- [43] F. Ustolin, N. Paltrinieri, F. Berto, Loss of integrity of hydrogen technologies: a critical review, *Int. J. Hydrog. Energy* 45 (2020) 23809–23840, <https://doi.org/10.1016/j.ijhydene.2020.06.021>.
- [44] J. Liu, M. Zhao, L. Rong, Overview of hydrogen-resistant alloys for high-pressure hydrogen environment: on the hydrogen energy structural materials, *Clean. Energy* 7 (2023) 99–115, <https://doi.org/10.1093/ce/zkad009>.
- [45] T. Ito, Y. Ogawa, W. Gong, T. Kawasaki, A. Shibata, S. Harjo, Stress and temperature, rather than hydrogen, govern stacking fault evolution during tensile deformation in Fe–24Cr–19Ni steel, *Scr. Mater.* 273 (2026) 117084, <https://doi.org/10.1016/j.scriptamat.2025.117084>.
- [46] T. Ito, Y. Ogawa, W. Gong, W. Mao, T. Kawasaki, K. Okada, A. Shibata, S. Harjo, Role of solute hydrogen on mechanical property enhancement in Fe–24Cr–19Ni austenitic steel: an *in situ* neutron diffraction study, *Acta Mater.* 287 (2025) 120767, <https://doi.org/10.1016/j.actamat.2025.120767>.
- [47] T. Perng, C.J. Altstetter, Effects of deformation on hydrogen permeation in austenitic stainless steels, *Acta Metall.* 34 (1986) 1771–1781, [https://doi.org/10.1016/0001-6160\(86\)90123-9](https://doi.org/10.1016/0001-6160(86)90123-9).
- [48] Y. Mine, T. Kimoto, Hydrogen uptake in austenitic stainless steels by exposure to gaseous hydrogen and its effect on tensile deformation, *Corros. Sci.* 53 (2011) 2619–2629, <https://doi.org/10.1016/j.corsci.2011.04.022>.
- [49] J. Yamabe, O. Takakuwa, H. Matsunaga, H. Itoga, S. Matsuoaka, Hydrogen diffusivity and tensile-ductility loss of solution-treated austenitic stainless steels with external and internal hydrogen, *Int. J. Hydrog. Energy* 42 (2017) 13289–13299, <https://doi.org/10.1016/j.ijhydene.2017.04.055>.
- [50] J.Z. Zhao, A.K. De, B.C. De Cooman, Kinetics of Cottrell atmosphere formation during strain aging of ultra-low carbon steels, *Mater. Lett.* 44 (2000) 374–378, [https://doi.org/10.1016/S0167-577X\(00\)00062-8](https://doi.org/10.1016/S0167-577X(00)00062-8).
- [51] J.-H. Kang, J.-M. Oh, Strain aging kinetics in FCC steels: site saturation vs matrix depletion, *Scr. Mater.* 274 (2026) 117140, <https://doi.org/10.1016/j.scriptamat.2025.117140>.
- [52] W.R. Cribb, R.E. Reed-Hill, Static strain-aging in nickel 200 between 373 and 473 K, *Metall. Trans. A* 8 (1977) 71–76, <https://doi.org/10.1007/BF02677266>.
- [53] S. Hartley, Strain-ageing in tantalum, *Acta Metall.* 14 (1966) 1237–1246, [https://doi.org/10.1016/0001-6160\(66\)90241-0](https://doi.org/10.1016/0001-6160(66)90241-0).
- [54] J.L. Martin, T. Krüml, Characterizing thermally activated dislocation mobility, *J. Alloys. Compd.* 378 (2004) 2–12, <https://doi.org/10.1016/j.jallcom.2003.10.063>.
- [55] F. Guin, P.L. Pratt, Stress relaxation and the plastic deformation of solids, *Phys. Status Solidi (B)* 6 (1964) 111–120, <https://doi.org/10.1002/pssb.19640060108>.
- [56] D. Lee, E.W. Hart, Stress relaxation and mechanical behavior of metals, *Metall. Trans. 2* (1971) 1245–1248, <https://doi.org/10.1007/BF02664258>.
- [57] R.M. Latanision, A.W. Ruff, The temperature dependence of stacking fault energy in Fe–Cr–Ni alloys, *Metall. Trans.* 2 (1971) 505–509, <https://doi.org/10.1007/BF02663341>.
- [58] X. Zhang, R. Takahashi, T. Akiyama, J. Yagi, Carburization rate into solid iron at CO-CO₂ atmosphere, *Tetsu-to-Hagane* 83 (1997) 299–304, <https://doi.org/10.2355/tetsuohagane1955.83.5.299>.
- [59] P. Thibaut, A. Métenier, C. Xhoffer, Carbon diffusion measurement in Austenite in the temperature range 500 °C to 900 °C, *Metall. Mater. Trans. A* 38 (2007) 1169–1176, <https://doi.org/10.1007/s11661-007-9150-5>.

- [60] M.I. Ismail, S.S. Iskander, E.B. Saleh, Carburizing of steels, *Surf. Technol.* 12 (1981) 341–349, [https://doi.org/10.1016/0376-4583\(81\)90028-5](https://doi.org/10.1016/0376-4583(81)90028-5).
- [61] S.-Y. Lee, S. Chettri, R. Sarmah, C. Takushima, J. Hamada, N. Nakada, Serrated flow accompanied with dynamic type transition of the Portevin–Le Chatelier effect in austenitic stainless steel, *J. Mater. Sci. Technol.* 133 (2023) 154–164, <https://doi.org/10.1016/j.jmst.2022.06.020>.
- [62] Y. Estrin, L.P. Kubin, Distribution of solute atoms round a slow dislocation, *Proc. R. Soc. L Math. Phys. Sci.* 199 (1949) 104–114, <https://doi.org/10.1098/rspa.1949.0128>.
- [63] Y. Estrin, L.P. Kubin, Local strain hardening and nonuniformity of plastic deformation, *Acta Metall.* 34 (1986) 2455–2464, [https://doi.org/10.1016/0001-6160\(86\)90148-3](https://doi.org/10.1016/0001-6160(86)90148-3).
- [64] T.H. Alden, Theory of mobile dislocation density: application to the deformation of 304 stainless steel, *Metall. Trans. A* 18 (1987) 51–62, <https://doi.org/10.1007/BF02646221>.
- [65] P.G. McCormick, A model for the Portevin–Le Chatelier effect in substitutional alloys, *Acta Metall.* 20 (1972) 351–354, [https://doi.org/10.1016/0001-6160\(72\)90028-4](https://doi.org/10.1016/0001-6160(72)90028-4).
- [66] A. Van Den Beukel, Theory of the effect of dynamic strain aging on mechanical properties, *Phys. Status Solidi(A)* 30 (1975) 197–206, <https://doi.org/10.1002/pssa.2210300120>.
- [67] N. Louat, On the theory of the portevin-le chatelier effect, *Scr. Metall.* 15 (1981) 1167–1170, [https://doi.org/10.1016/0036-9748\(81\)90290-8](https://doi.org/10.1016/0036-9748(81)90290-8).
- [68] L.P. Kubin, Y. Estrin, Evolution of dislocation densities and the critical conditions for the Portevin–Le Chatelier effect, *Acta Metall. Mater.* 38 (1990) 697–708, [https://doi.org/10.1016/0956-7151\(90\)90021-8](https://doi.org/10.1016/0956-7151(90)90021-8).
- [69] S.P. Hannula, M.A. Korhonen, C.Y. Li, Strain aging and load relaxation behavior of type 316 stainless steel at room temperature, *Metall. Trans. A* 17 (1986) 1757–1767, <https://doi.org/10.1007/BF02817274>.
- [70] M.A. Meyers, J.R.C. Guimarães, R.R. Avillez, On stress-relaxation experiments and their significance under strain-aging conditions, *Metall. Trans. A* 10 (1979) 33–40, <https://doi.org/10.1007/BF02686403>.
- [71] A. Atrens, N.F. Fiore, K. Miura, Dislocation damping and hydrogen pinning in austenitic stainless steels, *J. Appl. Phys.* 48 (1977) 4247–4251, <https://doi.org/10.1063/1.323410>.
- [72] Y. Yagodzinsky, M. Ivanchenko, H. Hänninen, Hydrogen-dislocation interaction in austenitic stainless steel studied with mechanical loss spectroscopy, *Solid State Phenom.* 184 (2012) 227–232, <https://doi.org/10.4028/www.scientific.net/SSP.184.227>.
- [73] X.W. Zhou, C. Nowak, R.S. Skelton, M.E. Foster, J.A. Ronevich, C. San Marchi, R. B. Sills, An Fe–Ni–Cr–H interatomic potential and predictions of hydrogen-affected stacking fault energies in austenitic stainless steels, *Int. J. Hydrog. Energy* 47 (2022) 651–665, <https://doi.org/10.1016/j.ijhydene.2021.09.261>.
- [74] J.P. Hirth, Effects of hydrogen on the properties of iron and steel, *Metall. Trans. A* 11 (1980) 861–890, <https://doi.org/10.1007/BF02654700>.
- [75] J.C. Fisher, On the strength of solid solution alloys, *Acta Metall.* 2 (1954) 9–10, [https://doi.org/10.1016/0001-6160\(54\)90087-5](https://doi.org/10.1016/0001-6160(54)90087-5).
- [76] J. Lothe, The effect of temperature on dislocations with condensed impurity atmospheres. Theory of dislocation motion and dislocation break-away, *Acta Metall.* 10 (1962) 663–670, [https://doi.org/10.1016/0001-6160\(62\)90133-5](https://doi.org/10.1016/0001-6160(62)90133-5).
- [77] P. Rodriguez, Serrated plastic flow, *Bull. Mater. Sci.* 6 (1984) 653–663, <https://doi.org/10.1007/BF02743993>.
- [78] J. Moriyama, O. Takakuwa, M. Yamaguchi, Y. Ogawa, K. Tsuzaki, The contribution of Cr and Ni to hydrogen absorption energy in Fe–Cr–Ni austenitic systems: a first-principles study, *Comput. Mater. Sci.* 232 (2024) 112650, <https://doi.org/10.1016/j.commatsci.2023.112650>.
- [79] J. Moriyama, M. Yamaguchi, O. Takakuwa, Effects of antagonistic interaction between Cr and Ni on hydrogen solubility in a Fe–Cr–Ni ternary austenitic system: a first-principles calculation, *Mater. Today Commun.* 40 (2024) 110059, <https://doi.org/10.1016/j.mtcomm.2024.110059>.
- [80] K. Oda, N. Kondo, K. Shibata, X-ray absorption fine structure analysis of interstitial (C, N)-substitutional (Cr) complexes in austenitic stainless steels, *ISIJ Int.* 30 (1990) 625–631, <https://doi.org/10.2355/isijinternational.30.625>.
- [81] J. Crank, *The Mathematics of Diffusion*, 2nd ed., Oxford University Press, New York, 1975.
- [82] Y. Ogawa, Temperature-sensitive ductilization in hydrogen-alloyed Fe–Cr–Ni austenitic steel by enhanced deformation twinning, *Scr. Mater.* 238 (2024) 115760, <https://doi.org/10.1016/j.scriptamat.2023.115760>.
- [83] Y. Ogawa, H. Nishida, O. Takakuwa, K. Tsuzaki, Hydrogen-enhanced deformation twinning in Fe–Cr–Ni-based austenitic steel characterized by in-situ EBSD observation, *Mater. Today Commun.* 34 (2023) 105433, <https://doi.org/10.1016/j.mtcomm.2023.105433>.
- [84] B.C. De Cooman, Y. Estrin, S.K. Kim, Twinning-induced plasticity (TWIP) steels, *Acta Mater.* 142 (2018) 283–362, <https://doi.org/10.1016/j.actamat.2017.06.046>.
- [85] H. Neuhäuser, H. Flor, Variation of obstacle strength during stress relaxation of α -brass single crystals, *Scr. Metall.* 12 (1978) 443–448, [https://doi.org/10.1016/0036-9748\(78\)90254-5](https://doi.org/10.1016/0036-9748(78)90254-5).
- [86] E.W. Hart, A phenomenological theory for plastic deformation of polycrystalline metals, *Acta Metall.* 18 (1970) 599–610, [https://doi.org/10.1016/0001-6160\(70\)90089-1](https://doi.org/10.1016/0001-6160(70)90089-1).
- [87] S.-P. Hannula, C.-Y. Li, Repeated load relaxations of type 316 austenitic stainless steel, *Scr. Metall.* 18 (1984) 225–229, [https://doi.org/10.1016/0036-9748\(84\)90512-X](https://doi.org/10.1016/0036-9748(84)90512-X).